4. MAGNETICS

Charles G. Bathke William P. Duggan William P. Kelleher
Farrokh Najmabadi Don Steiner

Contents

4. MAGNETICS

4.1. INTRODUCTION

The design points for the TITAN reversed-field-pinch (RFP) reactors (Table 3.6-I) were generated with the parametric systems model described in Section 3.2. The parametric systems analysis (PSA) model uses a simplified description of the magnet configuration illustrated in Figure 3.1-3 to estimate the magnet performance as characterized by the coil positions, masses, and ohmic losses summarized in Table 4.1-I. To advance the reactor design from the PSA level, the magnet design must be considered in more detail using the models described below. The coil parameters listed in Table 4.1-I provide design direction.

The magnet configuration consists of the following sets of coils: toroidal-field (TF), divertor-field (DF), and poloidal-field (PF) coils. The TITAN reactors operate at steady state using the oscillating-field current-drive (OFCD) system, which is described in Section 7. Rather than using a separate coil set to sustain the toroidal plasma current of $I_\phi \simeq 18$ MA, the TF, DF, and PF coils are oscillated about their steady-state currents and used as the OFCD driver coils. In addition, the TF coils provide the initial bias field, $B_{\phi o}$, on which the initial RFP configuration is formed. These coils subsequently maintain the external reversed field, $B_{\phi R}$, with a minimum ripple, $\Delta B_R/B_\theta$, at the plasma edge.

Two TITAN fusion power core (FPC) designs have been evaluated: (1) TITAN-I, a liquid-lithium, self-cooled design with vanadium-alloy (V-3Ti-1Si) structural material, and (2) TITAN-II, an aqueous-solution, self-cooled design with dissolved $LiNO_3$ salt as the breeder, and ferritic-steel alloy (9-C) as the structural material. The TITAN-II FPC is submerged in a pool of cold water to achieve passive safety. Two TF-coil design approaches were examined. The TITAN-I design uses the integrated-blanket-coil (IBC) concept [1], wherein poloidal currents are driven in the primary lithium coolant to produce the toroidal magnetic field (Section 4.2). The TITAN-II FPC design uses normal-conducting, Cu-alloy TF coils encasing the blanket, which is similar to the CRFPR design [2]. The TF-coil models, constraints, and designs are described in Section 4.3.

A magnetic divertor is used in conjunction with a highly radiating plasma to reduce peak heat loads on the divertor plate and also limit the sputtering rates to reasonable levels. The TITAN divertor nulls the minority toroidal field to minimize effects on the

Table 4.1-I.

SUMMARY OF PARAMETRIC SYSTEMS CODE ESTIMATES OF KEY PARAMETERS USED IN TITAN MAGNETICS DESIGNS[a]

Parameter	TITAN-I	TITAN-II
EF-coil option	SC	SC
DF-coil option	IBC[b]	Copper
TF-coil option	IBC[b]	Copper
Plasma Parameters		
Plasma current, I_ϕ (MA)	17.82	17.80
Major toroidal radius, R_T (m)	3.90	3.90
Plasma minor radius, r_p (m)	0.60	0.60
First-wall minor radius, r_p (m)	0.66	0.66
Reversed toroidal field, $B_{\phi R}$ (T)	− 0.382	− 0.381
Poloidal field at plasma surface, $B_\theta(r_p)$ (T)	5.94	5.93
Poloidal-Field Quantities		
OH-coil thickness, δ_{OH} (m)	0.27	0.37
Average minor radius of OH coil, r_{OH} (m)	1.56	1.37
Mass of OH-coil set, M_{OH} (tonne)	343.	414.
OH-coil current density, j_{OH} (MA/m^2)	13.1	9.2
OH-coil dissipation during back-bias (MW)	121.	107.
Mass of EF-coil set, M_{EF} (tonne)	305.	247.
EF-coil current density, j_{EF} (MA/m^2)	19.2	20.6
Toroidal-Field Quantities		
TF-coil thickness, δ_{TF} (m)	0.28	0.046
Average minor radius of coil, r_{TF} (m)	0.68	1.11
Mass of TF-coil set, M_{TF} (tonne)	41.	41.
TF-coil current density, j_{TF} (MA/m^2)	1.64	9.2
TF-coil dissipation, P^{Ω}_{TF} (MW)	27.6	13.6
Mass of DF-coil set, M_{DF} (tonne)	0.55	2.0
DF-coil dissipation, P^{Ω}_{DF} (MW)	142.	12.

(*a*) Section 3.6, Table 3.6-I.

(*b*) Integrated blanket coil (IBC) [1].

plasma and to minimize the DF-coil currents and ohmic losses. The DF coils also are designed to minimize toroidal-field ripple and are described in Section 4.4.

The PF-coil set performs an equilibrium and an ohmic-heating (start-up) function. The equilibrium function requires that a vertical field of appropriate magnitude, B_V, and index, $\partial(\ln B_V)/\partial(\ln R)$, corresponding to the values of the plasma current and beta [3 - 5] be imposed over the plasma cross section. The ohmic-heating function provides the poloidal-flux swing required to establish the steady-state plasma current, which is then subsequently sustained by OFCD. Since the ohmic-heating function is required only during start-up and the equilibrium function is required continuously, the PF-coil set is naturally, but not necessarily, separated into two sets of coils: equilibrium-field (EF) and ohmic-heating (OH) coils. This separation has also helped eliminate the need for on-site energy storage during the start-up procedure (Section 6). The OH- and EF-coil designs are described in Sections 4.5 and 4.6, respectively. A summary of the TITAN-I and TITAN-II magnet designs and conclusions are presented in Section 4.7.

4.2. INTEGRATED-BLANKET-COIL (IBC) CONCEPT

The integrated-blanket-coil (IBC) concept combines the blanket functions of tritium breeding and high-temperature energy recovery (of both fusion and ohmic heating) with the coil function of magnetic field production in a single component. The IBC resembles a conventional blanket sector, but the coolant also serves as the electrical conductor. The overall design is simplified by eliminating the coil shielding requirement and also the additional, but separate, coolant lines for the magnet coils found in conventional magnet designs. The IBC also improves reactor performance by increasing the tritium-breeding ratio (TBR) and energy recovery through a greater overall volume for capturing neutrons productively. Toroidal-field ripple can also be reduced.

Previous studies [1,6] indicate that adopting the IBC approach offers the following benefits:

- The IBC dual functions of coil and blanket permit a closer placement of the coil to the plasma without sacrificing neutronics performance, which potentially increases the mass power density of the FPC.
- Moving the coils closer to the plasma improves magnetic coupling as measured by inductance, thereby reducing current requirements in PF and DF coils.

- For compact reactors especially, the IBC simplifies design and maintenance because fewer coolant lines and the associated connections are required.

Several combinations of materials for the coolant (conductor) and the structure are possible for the IBC. The TITAN study has adopted an IBC based on liquid lithium and the vanadium alloy, V-3Ti-1Si. Liquid lithium is unique in combining cooling and tritium-breeding capability with high electrical conductivity relative to most blanket materials. Vanadium alloys are chemically compatible with liquid lithium and provide a suitable match of materials for use in the IBC.

One concern with the IBC concept is the large electrical resistivity of lithium relative to copper. If the concept is to be economically attractive, the joule losses should be comparable to those with a conventional resistive magnet system. However, even when a 70% fill fraction is assumed for a wound coil, the resistivity of the IBC is about 13 times larger than that of a room-temperature copper coil. Part of this difference is negated by capturing the ohmic heat in the blanket/coil, which serves as the main energy recovery component; therefore, about 40% of the resistive losses in the IBC reappear as electrical power, albeit added costs associated with added thermal-conversion capacity is incurred.

The IBC concept requires that the electrical and thermal hydraulic systems be physically connected, leading to relatively low-voltage, high-current (few-turn) coils. The coil leads carry large currents and require careful design to minimize the error fields and the power consumption therein. The design of the low-voltage, high-current power supplies is the most critical engineering issue for the IBC. The magnet engineering aspects of the TITAN IBCs are discussed in Section 10.5.

4.3. TOROIDAL-FIELD (TF) COILS

4.3.1. Models and Constraints

The major goal for the TF-coil design of RFPs is the achievement of minimal toroidal-field ripple. Toroidal-field ripple produces magnetic islands within the edge-plasma region. Particles and energy flow freely within this island structure, and plasma confinement is thereby degraded according to the island size. To ensure that confinement is not adversely affected by the TF ripple, the radial extent of the islands is required to be smaller than the radial distance between the reversal surface, r_r, and the plasma surface, r_p; this region is perceived to be primarily responsible for confinement in an RFP [7].

An estimate of the magnetic-island size produced by TF ripple is given in terms of the radial thickness of an island [8]:

$$\Delta r = 4 \left[\frac{r \, \Delta B_R}{n \, B_\theta \, (dq/dr)} \right]^{1/2} , \tag{4.3-1}$$

where r is the minor radius of the resonant surface, ΔB_R is the amplitude of the radial magnetic-field perturbation, n is the toroidal mode number of the perturbation, B_θ is the poloidal field at the resonant surface, and the derivative of the safety factor (dq/dr) is evaluated at the resonant surface. The safety factor at a given minor radius, r, is given by

$$q(r) = \frac{r \, B_\phi(r)}{R_T \, B_\theta(r)} , \tag{4.3-2}$$

where R_T is the plasma major toroidal radius and B_θ and B_ϕ are the poloidal and toroidal magnetic fields, respectively. In the case of TF ripple, the toroidal mode number of the perturbation is equal to the number of TF coils, N_{TF}. The resonant surface occurs, by definition, at the minor radius where the field lines and the magnetic-field perturbation have the same periodicity in the direction of the perturbation. Then the primary resonant surface for TF ripple occurs at the minor radius where $q(r) = N_{TF}^{-1}$, which in the limit of $N_{TF} \gg 1$ is approximated as r_r, the radius of the reversal surface where $B_\phi(r_r) = q(r_r) = 0$.

A circularized, 1-D ideal-MHD model described in Section 5.2 is used to determine r_r and dq/dr. The MHD model is based on the following specification of the current density parallel and perpendicular to the magnetic field:

$$\nabla \times \mathbf{B} = \mu_o \mathbf{j} = \mu_o (\mathbf{j}_\parallel + \mathbf{j}_\perp) , \tag{4.3-3}$$

$$\mathbf{j}_\parallel = \mu \mathbf{B} , \tag{4.3-4}$$

$$\mathbf{j}_\perp = \frac{\nabla p \times \mathbf{B}}{B^2} , \tag{4.3-5}$$

where Equation 4.3-3 is Ampere's law, Equation 4.3-4 gives the prescription for supporting a plasma pressure, p, in equilibrium, and Equation 4.3-5 invokes Taylor's hypothesis of the minimum energy state [9]. The MHD model requires as input the μ profile and the pressure profile. The pressure profile is derived from the assumed μ profile and from fits to density and temperature profiles calculated with the 1-D plasma simulations reported in Section 5.3. Given the poloidal beta, the plasma current, and either reversal or pinch parameters, the MHD model then determines the magnetic fields internal to the plasma,

Table 4.3-I.

PARAMETERS USED TO DETERMINE LOCATION OF REVERSAL SURFACE AND DERIVATIVE OF SAFETY FACTOR

Plasma current, I_ϕ (MA)	17.82
Plasma major toroidal radius, R_T (m)	3.9
Plasma minor radius, r_p (m)	0.6
Poloidal beta, β_θ	0.22
Reversal parameter, F	− 0.1
Pinch parameter, Θ	1.556
Reversal surface minor radius, r_r (m)	0.55
Reversal region thickness, $r_p - r_r$ (mm)	50.65
Edge-plasma safety factor, $q(r_p)$	− 0.0099
Safety factor derivative at reversal surface, $q'(r_r)$ (m^{-1})	− 0.3086

as shown in Figure 4.3-1, from which the q profile is derived. From the q profile, r_r and dq/dr are obtained and reported in Table 4.3-I. In addition, the B_θ profile indicates that the poloidal field at the resonant surface can be approximated conservatively by the poloidal field at the plasma edge. This approximation for B_θ permits the decoupling of design changes between TITAN-I and TITAN-II and the MHD calculation for r_r and dq/dr, which are relatively insensitive to the changes in I_ϕ.

The TF-coil designs for most RFP reactors [2] and experiments [10] strive for island widths $\Delta r \leq r_p - r_r$ which are achieved with ripples, ΔB_R, of a few mT produced by $N_{TF} \geq 25$ TF coils. The ripple for the TITAN TF-coil configurations is derived from 2-D field-line tracings at the plasma surface, where ΔB_R is slightly larger than at the resonant surface; the 3-D vacuum-field magnetics code, TORSIDO [11], is used with only the TF-coils simulated for this purpose.

In addition, the field errors produced by the gap in the IBC needed to permit the ingress and egress of the first-wall coolant channel and by the current leads to the single-

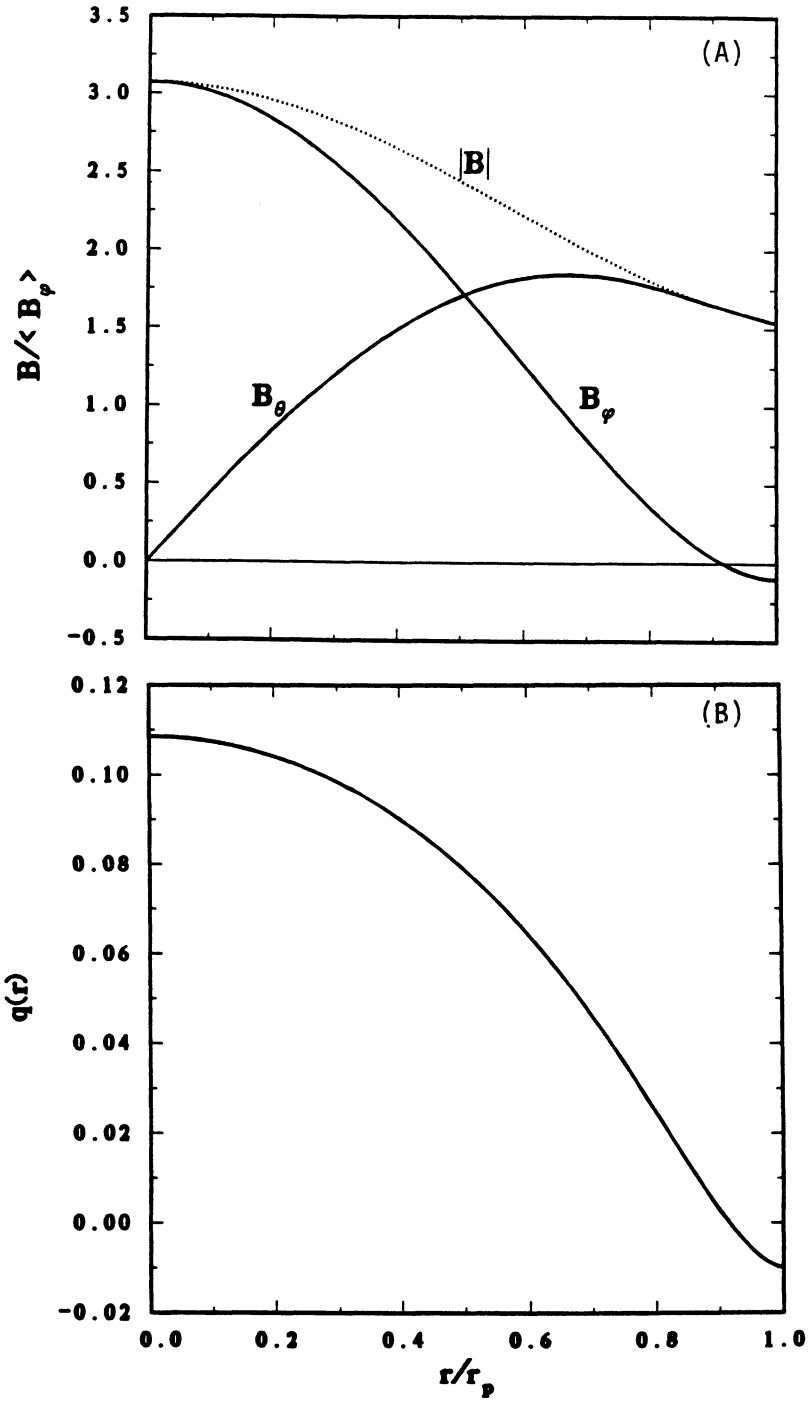

Figure 4.3-1. The radial profiles of (A) the magnetic field and (B) the safety factor, $q = (r/R)(B_\phi/B_\theta)$ from the 1-D MHD equilibrium model. These profiles are used to determine the location of the reversal surface, r_r, and $(dq/dr)_{r_r}$ for magnetic-island width estimates.

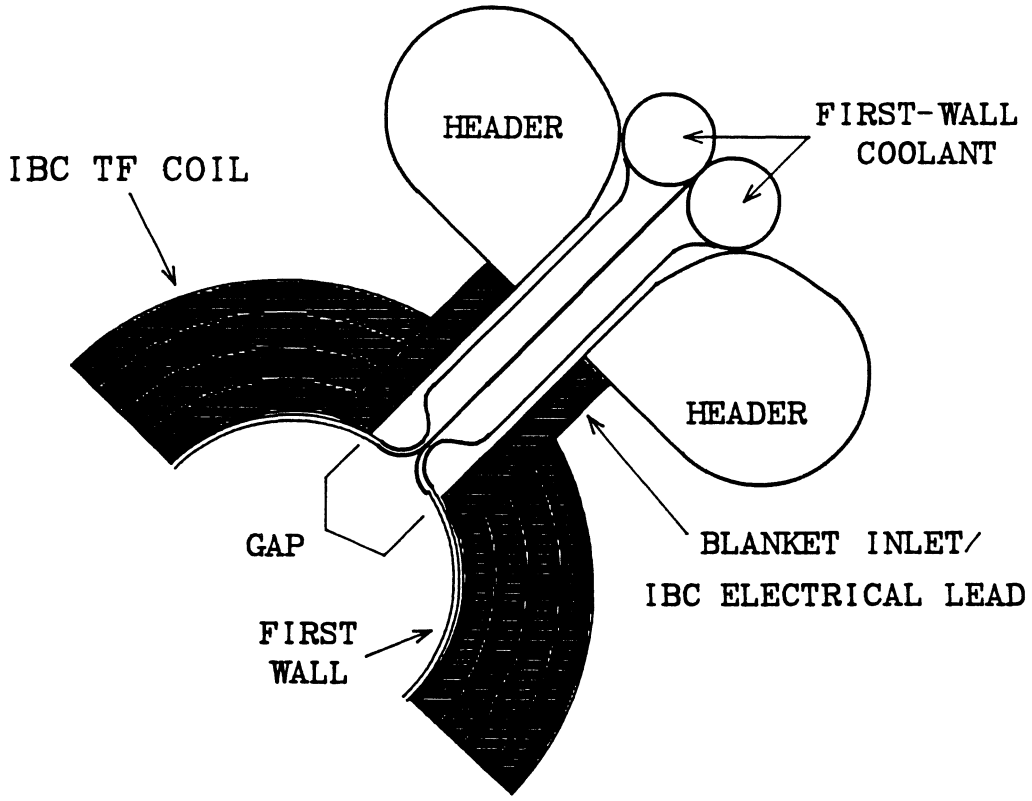

Figure 4.3-2. Schematic view of the IBC cross section, showing the electrical leads and the gap that are potential sources of field errors.

turn TF IBC, as shown in Figure 4.3-2, must also be minimized. The field-error constraint adopted is that the field errors be less than ΔB_R derived from the constraint imposed on magnetic-island widths. The IBC field errors are calculated with the 3-D magnetics code EFFI [12].

Additional constraints, summarized in Table 4.3-II, on the magnitude of the toroidal field and the geometry shown in Figure 4.3-3 are imposed on the TF-coil design. The coil geometry for TITAN-I is largely determined by thermal-hydraulic considerations (Section 10); the TF-coil design is analyzed only to verify compliance with the ripple and field-error constraints. For TITAN-II the coil geometry is mainly predetermined, with N_{TF} being the only degree of freedom. The TF-coil inner core radius is determined by blanket neutronics requirements. The blanket-coolant headers pass vertically through the space between TF coils, as is shown in Figure 4.3-3. Provision for these headers constrains the TF-coil "transparency" factor, which is defined as

$$f_{TF} = 1 - \frac{\ell_{TF}\, N_{TF}}{2\pi\, R_{TF}}, \tag{4.3-6}$$

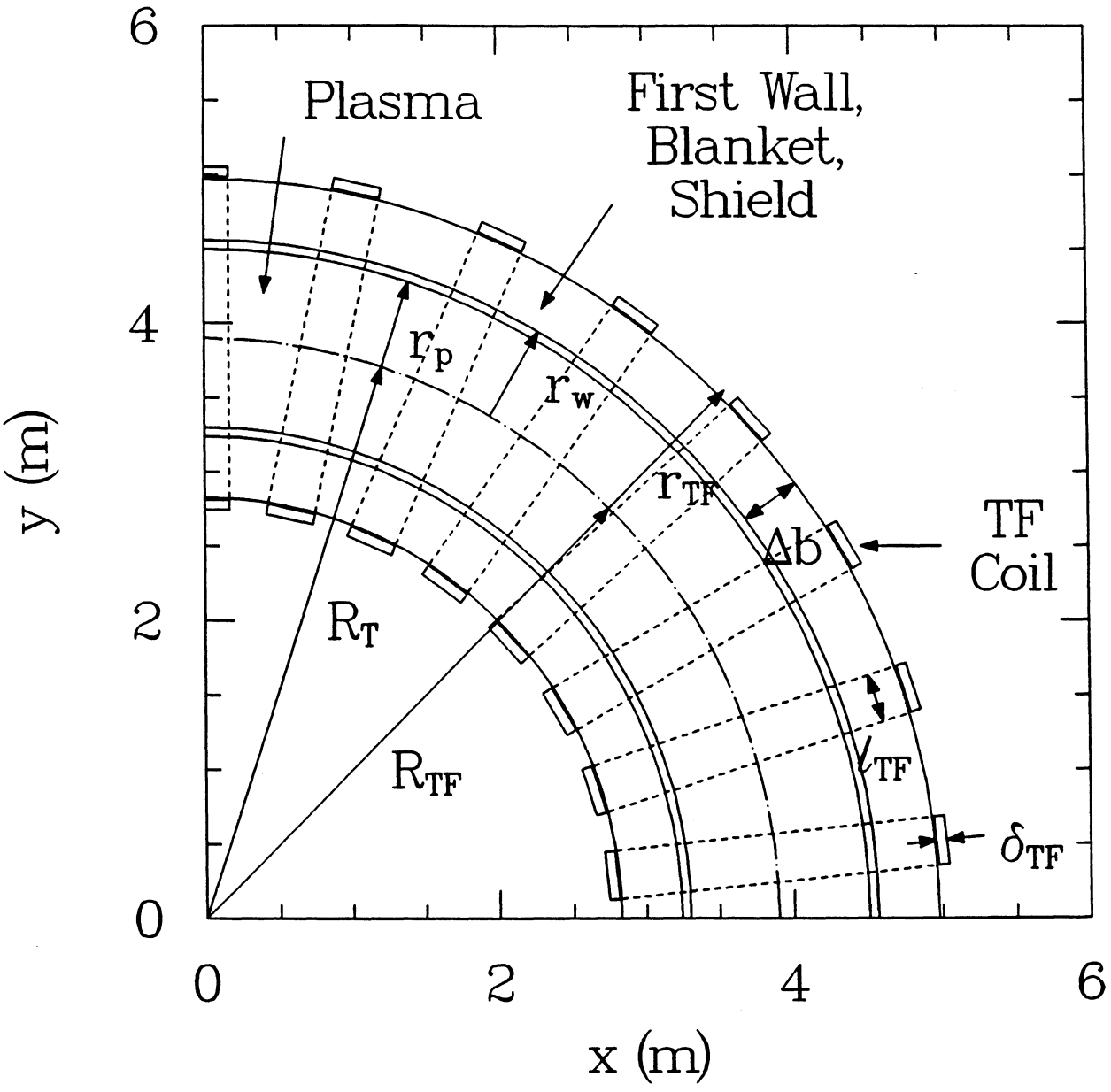

Figure 4.3-3. A schematic diagram of a conventional, Cu-alloy TF-coil design, indicating the notation used herein.

Table 4.3-II.

MAGNETIC FIELD AND GEOMETRY CONSTRAINTS IMPOSED ON TF-COIL DESIGN

Parameter	TITAN-I	TITAN-II
Reversed toroidal field, $B_{\phi R}$ (T)	− 0.36	− 0.38
Edge poloidal field, $B_\theta(r_p)$ (T)	5.60	5.91
Plasma-to-TF-coil clearance (m)	0.08	0.4825
TF-coil transparency factor, f_{TF}	0.0	0.6
Conductor fill fraction, λ	TBD[a]	0.7
TF-coil dissipated power (MW)	TBD[a]	16.
TF-coil major radius, R_{TF} (m)	3.9	TBD[a]
TF-coil minor radius, r_{TF} (m)	0.82	TBD[a]
TF-coil radial thickness, δ_{TF} (m)	0.28	TBD[a]

(a) These values are determined after TF-coil design is completed rather than serving as design constraints.

where ℓ_{TF} is the toroidal width of the TF-coil cross section and R_{TF} is the major radius of the coil, which may differ from R_T. The TF-coil dissipation is determined by cost optimization with the PSA model (Section 3.2). An additional constraint for TITAN-II is that N_{TF} be an integer multiple of the number of divertors to maintain symmetry of the divertors and ease of assembly and maintenance.

4.3.2. TITAN-I TF-Coil Design

For the interim TITAN-I TF IBC with a blanket thickness of 0.45 m, the amplitude of the ripple field was found to be a few μT, which in turn results in a magnetic-island width $\Delta r \leq 0.1$ mm for $N_{TF} \sim 10^3$ and is more than two orders of magnitude below the design constraint. Such a small ripple and, hence, island width is a result of the TF IBC being

an excellent approximation to a toroidally uniform conducting shell. The deviation from a shell is only a function of the diameter of the coolant tubes used in a TF IBC design and the spacing between the tubes. A close packing of the tubes is achieved by varying the tube cross section from a circle in the outboard equatorial plane to an ellipse which preserves the radial build in the inboard equatorial plane (Section 10). Since the final TF IBC design closely packs six radial rows of tubes in a radial build of 0.28 m as opposed to six rows in 0.45-m radial build for the interim design, the final design is expected to have even smaller ripple and island widths than the interim design. Consequently, TF ripple was judged not to be an issue for the TITAN-I TF-coil design given in Figure 4.3-4 and described in Table 4.3-III.

The current-element models of the TF IBCs, shown in Figure 4.3-5, were developed as input to EFFI [12] to calculate the error fields produced by the combination of gap and leads as shown in Figure 4.3-2. The current-element models are for the following ideal cases: no gaps or leads, for a gap of variable poloidal width but without lead, and a gap of variable width with leads forming a closed poloidal loop. Furthermore, the poloidal-current elements are modeled as 24 toroidally discrete coils of poloidally uniform cross section, as is shown in Figure 4.3-6, because of EFFI modeling limitations. Points A through F in Figure 4.3-5 mark the locations at which the fields are evaluated for the various cases. Points A and E are located at the plasma edge in the inboard and outboard midplane; B and D are located at the top and bottom plasma edges at the plasma major radius; C is located on the plasma minor axis; and F is located on the plasma edge at the gap center.

Possible error fields are: (1) perturbations to the toroidal field, (2) stray radial fields, and (3) stray vertical fields. Table 4.3-IV summarizes the results of the EFFI estimates of the toroidal-field strength for the various gap sizes. The cases with gaps but no leads produce significantly different toroidal fields compared to the calculated toroidal fields for the poloidally continuous cases of the "ideal loop" and the gap with leads. For example, at the plasma minor axis, point C, the ideal loop has a toroidal field of 0.364 T; the 54° gap has 0.323 T; and the 54° gap with leads has 0.362 T. Although the values are not exactly equal for the loop and gap with leads cases, they are sufficiently close to regard the differences as resulting from imperfections in the model geometry. These results indicate that the field topology within the plasma chamber is unaffected by the shape of the poloidal loop as long as the loop is closed, as is predicted by Ampere's law.

The same current-element models were used to evaluate the stray radial and vertical fields resulting from the gap and leads. The radial field in the "ideal loop" case is on the order of a few μT. As shown in Table 4.3-V, the cases with gap and leads have fields of

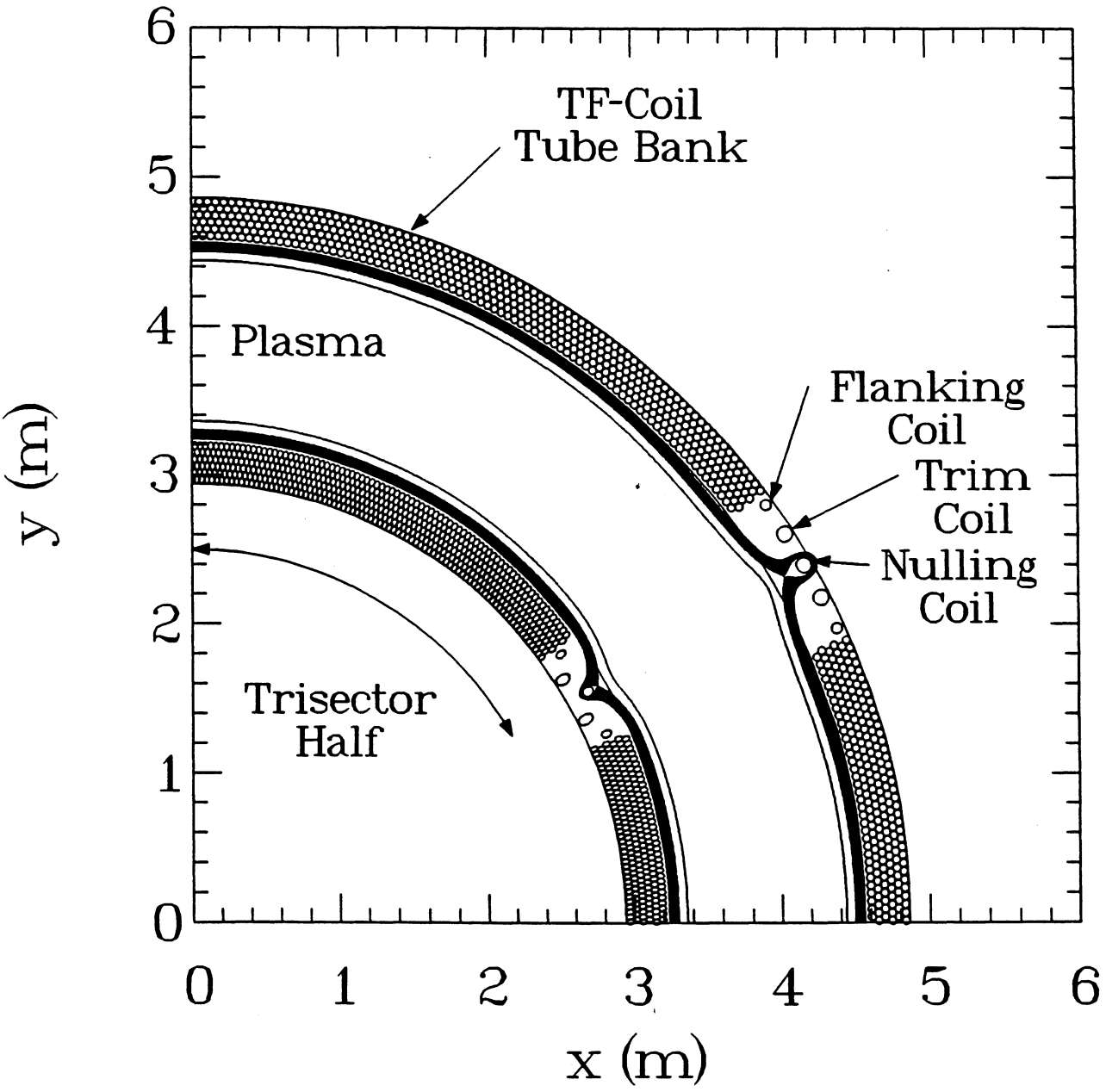

Figure 4.3-4. Equatorial-plane view of TF-IBC design with divertor. Also shown are field-line tracings at inboard and outboard minor radii of r = 0.5494, 0.5995, 0.6005, 0.6010, 0.6030, 0.6060, 0.6090, 0.6120, 0.6180, 0.6240, 0.6300, 0.6360, 0.6420, 0.6480, 0.6540, and 0.6600 m.

Table 4.3-III.

PARAMETERS OF TITAN-I TOROIDAL-FIELD COILS

Current per trisector (MA)	2.08					
Reversed toroidal field, $B_{\phi R}$ (T)	0.36					
Number of tubes per trisector	975					
Average current per tube (kA)	2.13					
Tube inner diameter (mm)[a]	47.5					
Tube wall thickness (mm)[a]	2.5					
Tube inner area (m^2)	1.40×10^{-3}					
Average current density (MA/m^2)	1.52					
Resistivity, η ($\mu\Omega$-m)	0.353					
Total power, P_{TF}^{Ω} (MW)	24.0					
Blanket coverage	0.887					

Tube data for row number:	**1**	**2**	**3**	**4**	**5**	**6**
Poloidal radius, $r_{\theta c}$ (m)	0.706	0.752	0.797	0.843	0.888	0.934
Number per trisector	162	163	162	163	162	163
Current, $I_{\theta c}$ (kA)	2.22	2.19	2.15	2.11	2.08	2.04
Current density $\langle j_{\theta c} \rangle$ (MA/m^2)	1.54	1.54	1.53	1.52	1.52	1.51

(a) Values evaluated at outboard equatorial plane and vary poloidally.

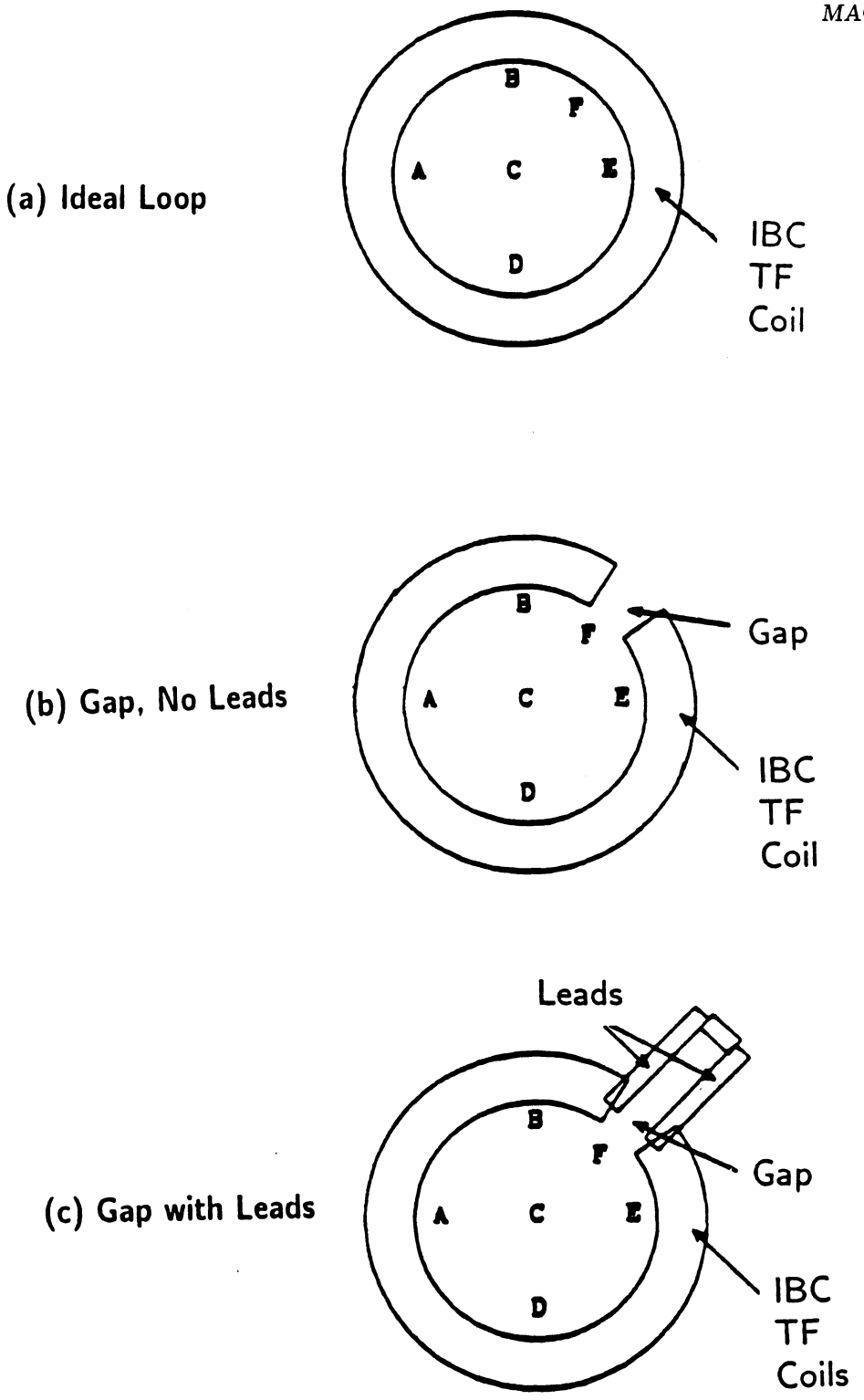

Figure 4.3-5. A schematic view of the poloidal cross section of current-element models inputted to EFFI to evaluate field errors for the TF IBCs. Also shown are the locations where field errors are calculated.

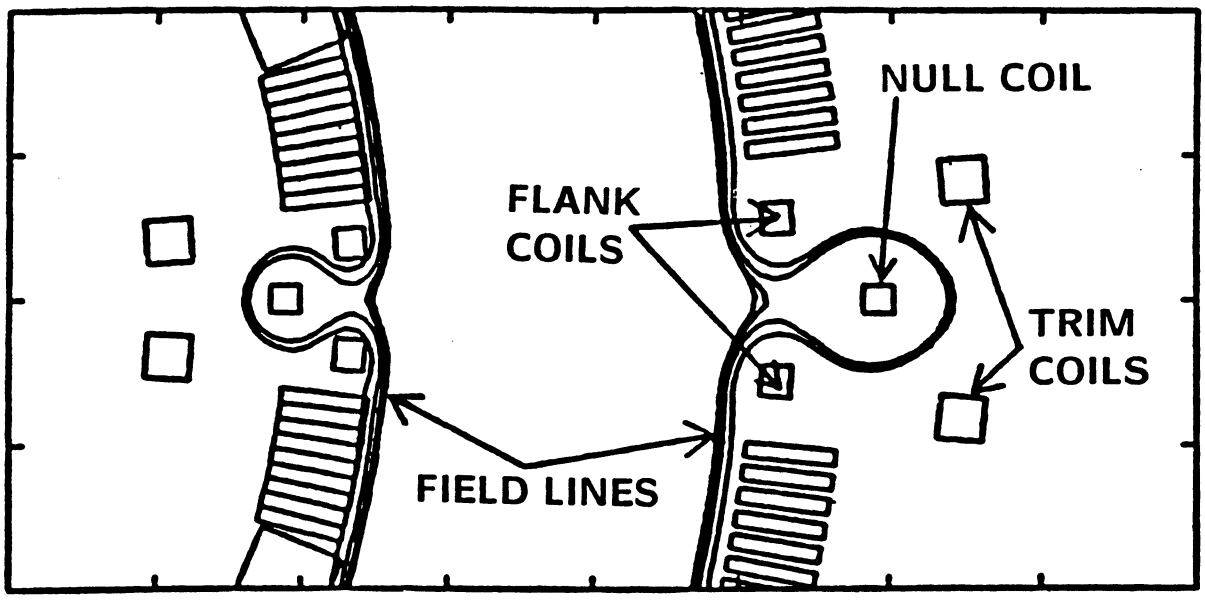

Figure 4.3-6. A schematic view of the toroidal cross section of the current-element models inputted to EFFI to evaluate field errors for the TF IBCs. Also shown are divertor coils.

similar magnitude. The stray vertical fields, also listed in Table 4.3-V, are even smaller ($\sim$ 1 to 2 μT). The TF-ripple constraint calculated for TITAN allows a spatial radial-field variation of a few mT. In this context, the μT fields generated by the leads are insignificant. This conclusion is especially true when compared to the poloidal fields of several tesla generated by the plasma and PF coils.

4.3.3. TITAN-II TF-Coil Design

As discussed in Section 4.3.1, the TITAN-II geometry is specified to the point that the only degree of freedom in designing the TF coils is N_{TF}. The total TF-coil cross-sectional area is independent of N_{TF} because the magnetic field and the power dissipation are held constant near values suggested by the PSA as being nearly minimum COE. The toroidal width, ℓ_{TF}, of a single TF coil varies inversely with N_{TF} and the radial thickness, δ_{TF}, of a TF coil is independent of N_{TF}, because the TF-coil transparency factor, f_{TF}, is also constant. Because ℓ_{TF} is varying, the TF-coil major and minor radii (respectively, R_{TF} and r_{TF}) must change with N_{TF} to provide a constant plasma-to-TF-coil clearance in

Table 4.3-IV.

TOROIDAL FIELD CALCULATED FOR VARIOUS CURRENT-ELEMENT MODELS OF TITAN-I TOROIDAL-FIELD IBC[a]

Case	Toroidal Field (T) at Location [a]					
	A	B	C	D	E	F
Ideal loop	0.424	0.385	0.364	0.386	0.362	0.364
10° gap	0.420	0.378	0.364	0.382	0.355	0.327
22° gap	0.415	0.369	0.348	0.378	0.346	0.289
54° gap	0.402	0.337	0.323	0.366	0.315	0.226
10° gap and leads	0.423	0.382	0.362	0.385	0.358	0.361
22° gap and leads	0.422	0.379	0.362	0.384	0.356	0.361
54° gap and leads	0.422	0.374	0.362	0.384	0.349	0.353

(a) For the current-element models and gaps shown in Figure 4.3-5.

toroidal geometry. This clearance is measured in the coil midplane on the outboard side of the equatorial plane and along a ray from the plasma major axis which passes through a corner of the TF-coil cross section on the coil inner surface on the inboard side of the equatorial plane, resulting in a slight inward shift of the TF coil relative to the plasma minor axis.

The results of the ripple calculations over a range of N_{TF} values are presented in Table 4.3-VI and Figure 4.3-7. The amplitude of the ripple field, ΔB_R, decreases with increasing N_{TF} so that the magnetic island width, Δr, falls off faster than the explicit prediction of Equation 4.3-1 that $\Delta r \propto N_{TF}^{-1}$; this behavior is shown in Figure 4.3-7. The TITAN-II TF-coil design described in Table 4.3-VII and shown in Figure 4.3-3 meets the magnetic-island constraint with only a small safety margin. The safety margin could be increased if so desired by increasing the plasma-to-TF-coil clearance and the TF-coil minor radius as illustrated by results in Figure 4.3-7 for a 65-mm larger value of r_{TF}.

Table 4.3-V.

STRAY FIELD CALCULATED FOR VARIOUS CURRENT-ELEMENT MODELS OF TITAN-I TOROIDAL-FIELD IBC[a]

Case	Stray Field (μT) at Location [a]					
	A	B	C	D	E	F
			Stray Radial Field			
Ideal loop	9.701	5.899	6.605	5.899	0.832	2.524
10° gap	9.621	5.957	6.672	5.971	1.056	2.715
22° gap	9.523	6.026	6.754	6.057	1.330	2.940
54° gap	9.280	6.208	6.964	6.274	2.020	3.501
10° gap and leads	8.365	4.041	4.953	4.743	0.954	0.573
22° gap and leads	7.303	4.110	3.733	3.547	2.523	0.334
54° gap and leads	8.237	4.299	5.277	5.235	0.241	1.028
			Stray Vertical Field			
Ideal Loop	0.	2.005	0.	2.005	0.	1.820
10° gap	0.169	2.088	0.071	1.957	0.093	1.771
22° gap	0.369	2.181	0.151	1.904	0.208	1.706
54° gap	0.864	2.327	0.288	1.803	0.562	1.443
10° gap and leads	0.787	0.366	1.336	2.932	1.718	0.054
22° gap and leads	1.115	0.874	1.467	3.159	1.585	0.451
54° gap and leads	0.579	0.947	0.789	2.399	2.662	0.812

(a) For the current-element models and gaps shown in Figure 4.3-5.

Table 4.3-VI.

RESULTS OF TITAN-II RIPPLE CALCULATIONS

N_{TF}	ΔB_R (mT)	Δr (mm)	$\mid r_O - r_I \mid$ (mm)	ℓ_{TF} (mm)	Δ_{TF} (mm)	R_{TF} (m)	r_{TF} (m)
24	27.72	74.65	28.69	408.3	70.5	3.896	1.121
27	19.72	59.36	18.34	363.1	70.4	3.897	1.121
30	14.14	47.69	11.96	326.7	70.4	3.898	1.120
33	10.16	38.55	7.90	297.1	70.4	3.898	1.120
36	7.37	31.43	5.30	272.2	70.3	3.898	1.119
39	5.28	25.56	3.53	251.3	70.3	3.899	1.119

Cost penalties associated with an increase in coil mass, obviously, result from exercising this option.

The magnetic-island width predicted by Equation 4.3-1 is not valid because the resonant surface (where $q(r) = N_{TF}^{-1}$) does not lie between r_r and r_p. Three-dimensional field-line tracings in the plasma edge region with the TF and PF coils and plasma simulated under the same conditions of non-resonance of the TF ripple [13] indicate that the magnetic island width or flux surface broadening is the same as the difference, $\mid r_O - r_I \mid$, in the radial amplitudes of outboard and inboard field-line tracings in two dimensions with only the TF coils simulated. The island widths in this case are ~ 0.2 of the constraint, as is indicated in Table 4.3-VI.

The sensitivity of the TF-coil thickness to the ohmic dissipation constraint is explored in Figure 4.3-8 for the parameters listed in Table 4.3-VI. The design point occurs at the knee of the dissipation versus thickness curve indicating a cost balance between power dissipation and coil mass. Changing the TF-coil thickness has little effect on island widths for a given N_{TF}, but a variation in thickness would change f_{TF}. A self-consistent changing of the ohmic-dissipation constraint which affects the TF-coil thickness would then change N_{TF}. Changes to N_{TF} are compounded by the requirement that N_{TF} be an integer multiple of the number of divertors.

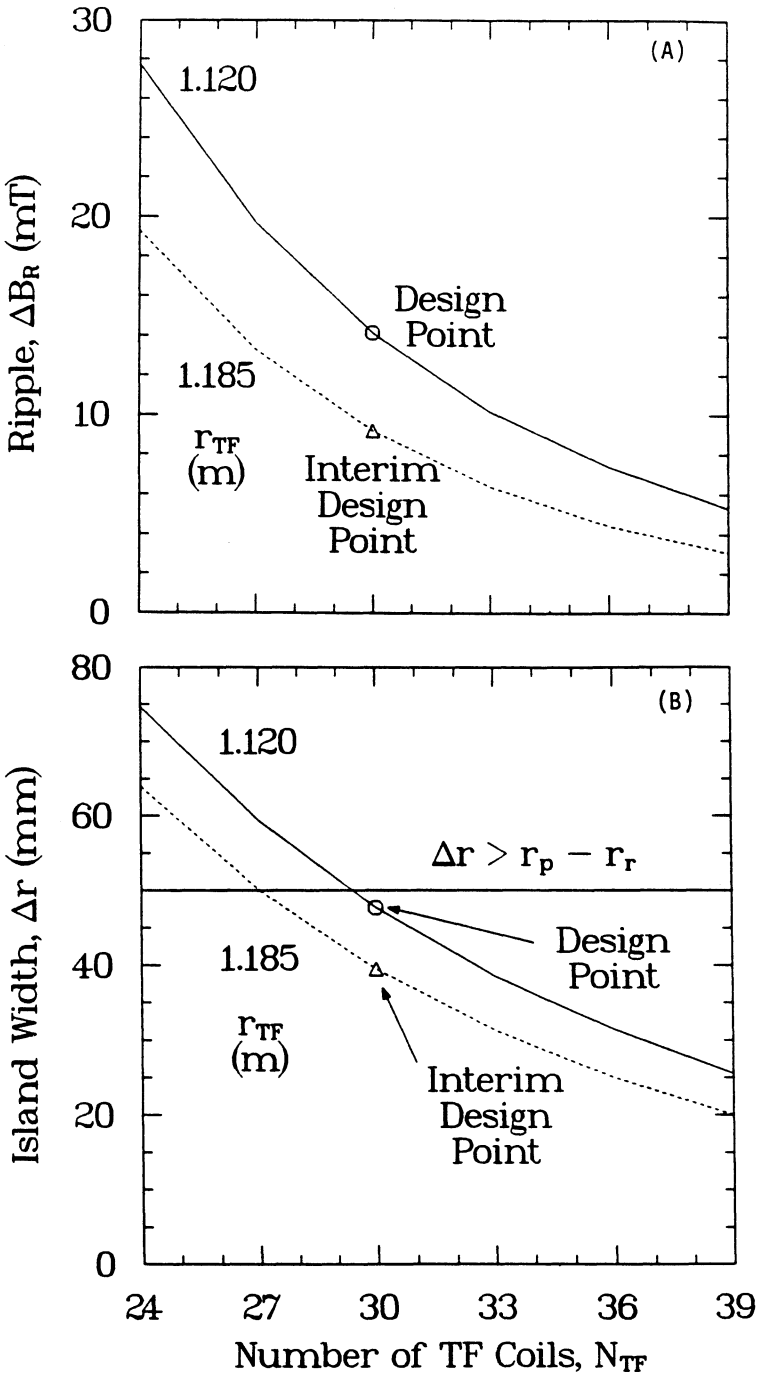

Figure 4.3-7. Amplitude of the ripple magnetic field (A) and the corresponding magnetic-island widths (B) as functions of the number of TF coils, N_{TF}. Also shown are results for an interim design point illustrating the effect of changing the plasma-to-TF-coil clearance by 65 mm.

Table 4.3-VII.

PARAMETERS OF TITAN-II TOROIDAL-FIELD COILS

Number of TF coils, N_{TF}	30.
Major radius, R_{TF} (m)	3.898
Minor radius, r_{TF} (m)	1.120
Radial thickness, δ_{TF} (mm)	70.4
Toroidal thickness, ℓ_{TF} (mm)	326.7
Reversed toroidal field, $B_{\phi R}$ (T)	0.38
Current per coil, I_{TF}/N_{TF} (kA)	247.0
Current density, j_{TF} (MA/m^2)	10.7
Steady-state peak coil field, $B_{\phi c}$ (T)	0.69
TF-coil mass, M_{TF} (tonne)	35.5[a]
Total ohmic power, P^{Ω}_{TF} (MW)	16.

(a) Assuming a coil density of 7.3 tonne/m^2.

4.4. DIVERTOR-FIELD (DF) COILS

4.4.1. Models and Constraints

The divertor design approach adopted by the TITAN study builds directly on the results of References [13 - 16]. The divertor nulls the minority toroidal field to minimize perturbations to the confining magnetic field in the plasma and to minimize the DF-coil currents required to produce a null. The TF null is a line poloidally encircling the plasma cross section upon which the toroidal field is zero. The plasma surface is taken to be the separatrix, which is the boundary differentiating open (leaving the plasma chamber) and closed (contained within the plasma surface) field lines. The separatrix surface also contains the null. The null is produced by a nulling coil, as is shown in Figure 4.3-4. The nulling coils (one per divertor location) form a solenoid within the TF-coil solenoid; the

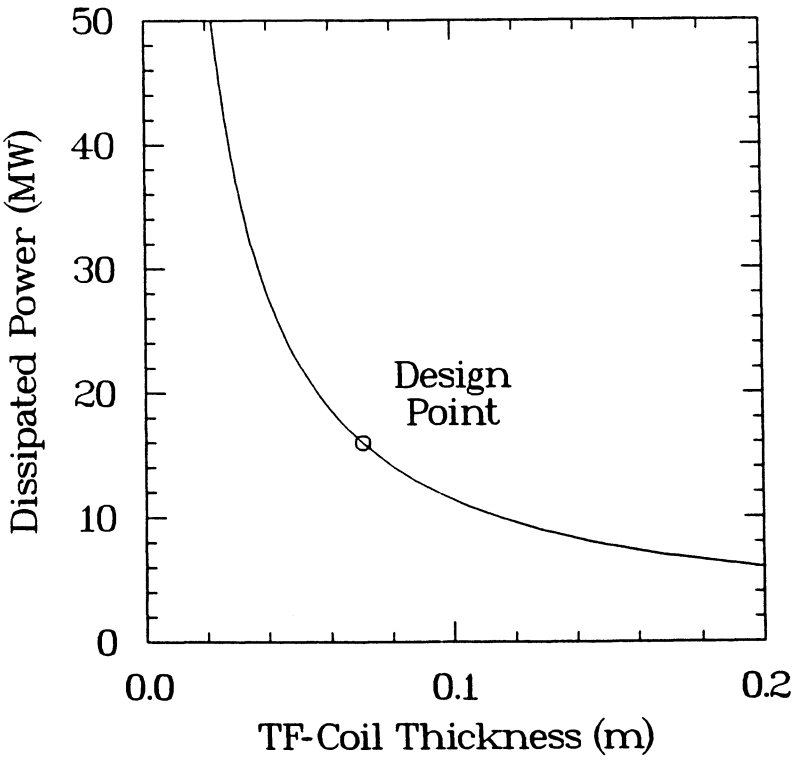

Figure 4.3-8. Sensitivity of the TF-coil ohmic dissipation to changes in coil thickness for the parameters of Table 4.3-VII.

nulling-coil solenoid nearly cancels the toroidal field over the volume of the inner solenoid. To localize the effect of the nulling coil, two flanking coils are positioned symmetrically about the nulling coil, as is shown in Figure 4.3-4. The flanking coils carry a combined current equal to that in the nulling coil, but of opposite sign. In the case of the IBC divertor, the divertor assembly displaces a portion of the IBC TF-coil tube bank. A pair of trim coils is required to conduct a current equal to that of the displaced tube bank in order to control the TF ripple.

Particles and energy diffuse across the separatrix, creating a plasma exhaust that flows along the open field lines to the divertor or diffuses across field lines to the first wall. The open field lines form a plume that encircles the nulling coil upon entering the divertor region. A neutralizer or collector plate is positioned to intercept the plasma exhaust confined to the field-line plume.

Two divertor configurations are possible depending on the location of the collector plate: a closed divertor and an open divertor. The collector plate in the closed divertor

is positioned to intercept the plume at the furthest possible location from the plasma in order to inhibit neutral particles from entering the plasma because of the remoteness of the point of interaction between the plate and the plasma exhaust. In the open divertor approach, the plate is positioned near the null, requiring several neutral mean free paths (four are assumed sufficient here) between the plate and the separatrix to prevent the neutral particles from entering the plasma.

The open divertor has a decided advantage over a closed divertor in an RFP because adjacent field lines are decompressed near the null and compressed at the outermost part of the plume relative to the spacing of adjacent field lines far away from a divertor. This decompression of field lines causes a substantial decrease in the heat and particle fluxes incident upon the plate in the open divertor relative to the closed divertor. Furthermore, a poloidal asymmetry in the field-line density exists in the plume which is negligible at the null and increases monotonically to a maximum at the outermost point of the plume. This asymmetry enhances the differences in peak heat and particle fluxes between the two approaches with the open divertor showing less poloidal asymmetry. Consequently, the open divertor approach was adopted for the TITAN divertor designs.

The divertor magnetic topology is determined with the 3-D vacuum magnetics code TORSIDO [11], but only 2-D field lines confined to the equatorial plane are traced, with only the TF and DF coils being simulated. The more economical 2-D field-line tracings were found to reproduce the 3-D field-line tracings in the portion of the scrape-off layer (SOL, the open field-line region between the separatrix and first wall) of interest for an open divertor. A flux-surface expansion factor that measures the expansion or compression of adjacent field lines relative to the spacing at the divertor midplane is also calculated along a field line. The calculation of the flux-surface expansion factor appropriately assumes that the flux in the equatorial plane is constant along a field line; this factor is then simply the ratio of the magnitude of the field at the divertor midplane (toroidal and radial components only) to the magnitude of the local field.

A 3-D field-line length, L, is also calculated by

$$L = \int \frac{(B_V^2 + B_\phi^2 + B_R^2)^{1/2}}{(B_\phi^2 + B_R^2)^{1/2}}\, dl\,, \tag{4.4-1}$$

where dl is the integration step size in the equatorial plane for the 2-D field-line tracings. The vertical field in the equatorial plane is B_V and is produced by EF coils (positioned as in the TITAN-I design described in Section 4.6.1) and by the plasma, which is simulated with a hoop current at a major radius of $R_T^* = 3.908\,\mathrm{m}$ to account for the Shafranov shift [10]. The magnetic fields B_ϕ and B_R are the toroidal and radial fields produced by

the TF and DF coils. Field-line lengths from the divertor midplane to the null, L_N, and to the plate, L_p, are calculated specifically for use in the edge-plasma modeling discussed in Section 5.4. The field-line coordinates for field-line tracings from the divertor midplane to a point past the divertor at minor radii of 600.5, 601.0, 603.0, 606.0, 609.0, 612.0, 618.0, 624.0, 630.0, 636.0, 642.0, 648.0, 654.0 and 660.0 mm in the SOL are tabulated for use in the divertor-plate design (Section 11.4). In addition, the magnetic field components, the flux-surface expansion factors, and field-line lengths corresponding to the above field-line coordinates are included in the divertor tabulations.

The divertor magnetics connection to edge-plasma modeling and target design was exercised iteratively to establish divertor performance criteria. The TITAN-I and TITAN-II target designs have different critical heat-flux limits set by the choice of coolant, structural material, and configuration. The critical heat-flux limits translate into magnetics requirements that the TITAN-I divertor design produce a peak flux-surface expansion factor of ~ 2 at a plate location 22.1 mm (four neutral mean free paths) from the null. The TITAN-II divertor design produces an expansion factor of ~ 3. Only three divertors are used in either design. Production of a higher flux-surface expansion factor requires a larger nulling-coil minor radius resulting in a larger ohmic dissipation in the divertor coils. Reactor economics, which in turn is driven by the thermal-energy conversion efficiency, η_{TH}, restricts the divertor ohmic dissipation to $P_{DF}^{\Omega} \simeq 100\,\mathrm{MW}$ for TITAN-I and to $P_{DF}^{\Omega} \simeq 10\,\mathrm{MW}$ for TITAN-II. The ohmic dissipation is affected by the angular spread between flanking and nulling coils which, in turn, affects the ripple produced by the divertor. The divertor ripple is large, but this ripple is also characterized by a high mode number (Equation 4.3-1). A 3-D analysis of the divertor ripple in the CRFPR [13] at parameters similar to TITAN indicates that a 4° spacing between the flanking and nulling coils produces magnetic islands smaller than those produced by the TF coils. Consequently, a 4° spacing was adopted as a guideline in the TITAN design to meet the ripple constraint. In addition, symmetrizing the edge-plasma region ($r_r \leq r \leq r_p$) from inboard to outboard was found to play an important role in reducing divertor-introduced island widths and is imposed as an additional goal.

The location of the divertor coils consistent with the above constraints is determined by the following algorithm. The nulling coil is located close to the plasma on the inboard side to minimize the divertor-coil current and to obtain acceptable flux-surface expansion factors. The outboard locations of all divertor coils are determined by requiring an inboard/outboard symmetry of the edge-plasma region. The divertor coils also are constrained to remain inside the blanket envelope in order not to displace shielding. The flanking coils are positioned to minimize TF ripple. The trim coils required in the

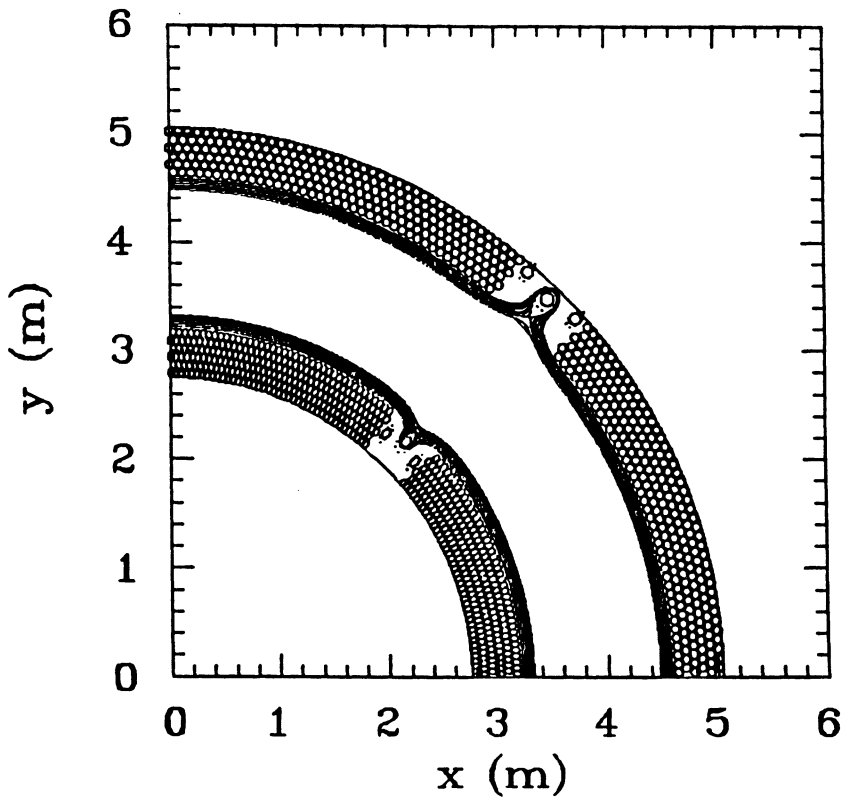

Figure 4.4-1. The divertor configuration for Case I of the nulling-coil radial-position sensitivity study summarized in Table 4.4-I.

TITAN-I IBC design are positioned radially as far as possible from the nulling coil within the blanket envelope to minimize the divertor currents; the toroidal position minimizes TF ripple when operated without the divertor as in the RFP formation phase.

4.4.2. TITAN-I DF-Coil Design

The higher resistivity of Li ($0.35\,\mu\Omega\,\mathrm{m}$) relative to Cu ($0.02\,\mu\,\Omega\,\mathrm{m}$) results in a large ohmic dissipation for divertor IBCs. Because of spatial restrictions imposed by the target design, the DF-coil cross-sectional area cannot be increased sufficiently to achieve a tolerable ohmic dissipation. Management of the IBC divertor ohmic dissipation was investigated first with a study of the impact of radial variations of the nulling coil, as reported in Table 4.4-I. The DF- and TF-coil configurations corresponding to the three cases in Table 4.4-I are shown in Figures 4.4-1 and 4.4-2 with the flanking and trim coils combined. The DF coils are shown with two cross sections. The ohmic dissipation for the smaller cross section was evaluated with a Cu-like resistivity. The second cross section

Table 4.4-I.

TITAN-I DIVERTOR COILS SENSITIVITY STUDY

Parameter	Case I	Case II	Case III
Nulling coil:			
Current (MA)	- 0.331	- 0.705	- 1.7098
Current density (MA/m^2) [a]	30.0 (37.0)	30.0 (37.8)	30.0 (38.4)
Major radius (m)	3.9847	4.0152	4.0162
Minor radius (m)	0.9327	1.0392	1.1262
Cross-sectional radius (mm)	59.3	86.49	134.69
Radius enlargement factor	1.9	2.1	1.7
Flanking coil:			
Current (MA)	0.263	0.45	0.9524
Current density (MA/m^2)[a]	30.0 (37.5)	30.0 (37.7)	30.0 (37.9)
Major radius (m)	3.983	4.0	3.978
Minor radius (m)	0.9960	1.025	1.048
Cross-sectional radius (mm)	52.83	69.10	100.53
Ohmic losses (MW):			
Cu ($\eta = 0.020\,\mu\Omega$-m)	22.3	44.8	107.4
Li ($\eta = 0.347\,\mu\Omega$-m)	117.8	199.2	611.3
Inboard null minor radius (m)	0.725	0.728	0.729
Shielding thickness (mm)	64.	110.	146.
Flux surface expansion factor (at $r = 0.6005$ m):			
Inboard	3.41	3.89	4.85
Outboard	5.59	6.19	5.87
Divertor connection lengths (m) (at $r = 0.6005$ m):			
Inboard	42.9	46.0	46.7
Outboard	71.6	73.2	75.0
Average	57.2	59.6	60.8

(a) Values in the outboard equatorial-plane cross section. Poloidally averaged values are listed in parenthesis.

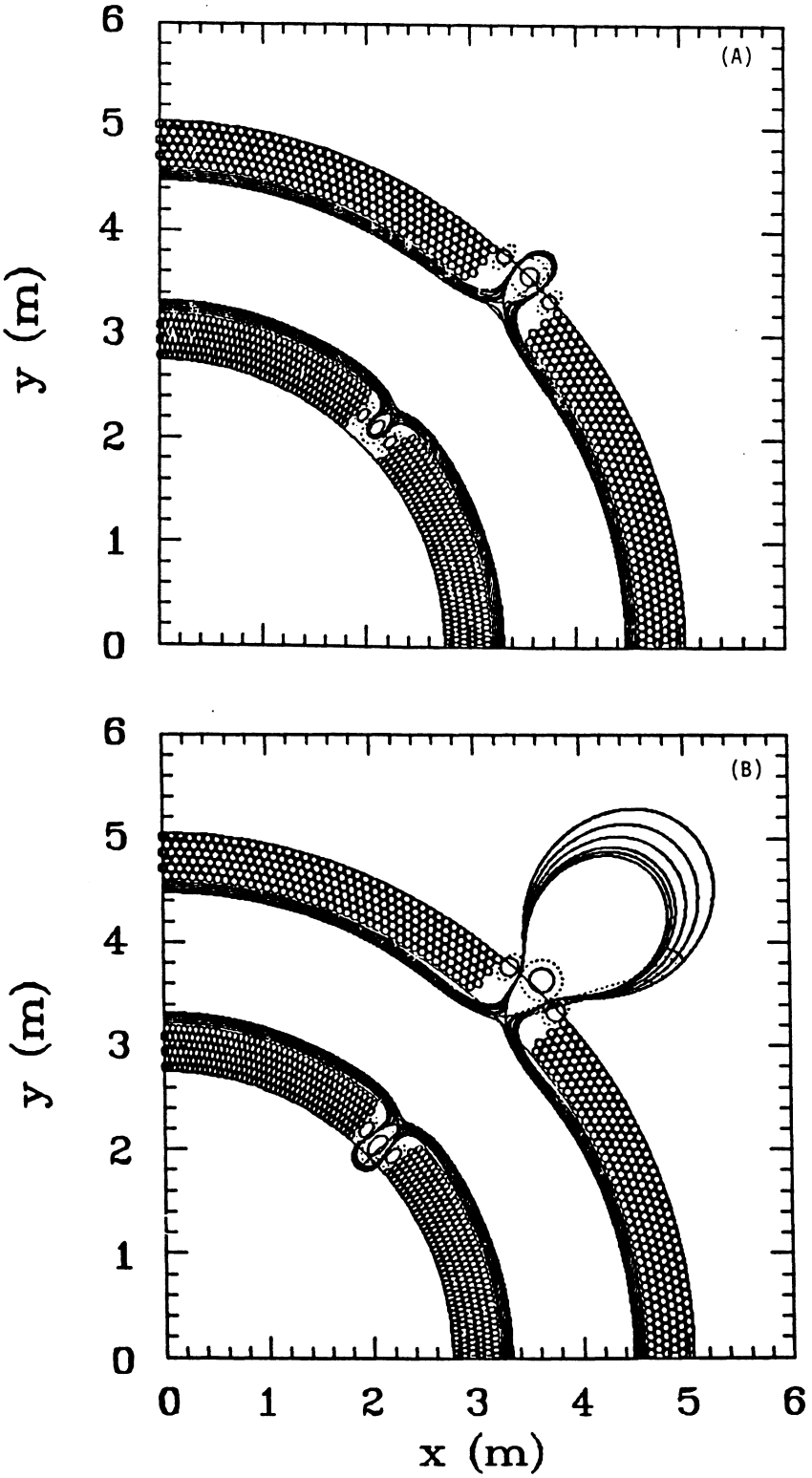

Figure 4.4-2. The divertor configuration for Case II (A) and Case III (B) of the nulling-coil radial-position sensitivity study summarized in Table 4.4-I.

represents the largest cross section possible in the design. The increase in cross-sectional area can be gauged from the radius enlargement factor listed in Table 4.3-I. This factor is applied uniformly to the nulling coils, but only radially to the flanking coils which creates elliptical cross sections at both inboard and outboard positions. The enlargement factor is bounded by the null at the inboard equatorial plane or the flanking coils. With the enlarged cross sections, only Case III has room between the nulling coil and the null for a collector plate with a shape that reduces the peak heat flux to an acceptable level ($\leq 100\,\mathrm{MW/m^2}$). However, the ohmic dissipation evaluated for a Li-like resistivity in the larger cross section for Case III is unacceptable. The space between the null and the smaller cross sections is tabulated in Table 4.4-I as an available shielding thickness. Based on the shielding thicknesses and ohmic losses reported in Table 4.4-I, a copper DF-coil solution is possible with $\sim 4°$ spacing between the flanking and nulling coils. However, the IBC option was adopted for both the TF and DF coils.

The resulting divertor design is shown in Figure 4.3-4 and described in Table 4.4-II. The angular spread between the flanking and nulling coils had to be increased to 5.7° to achieve a peak flux-surface expansion factor of ~ 2 at the collector plate and an ohmic dissipation of $\sim 120\,\mathrm{MW}$. An expanded view of the divertor region is shown in Figure 4.4-3, which illustrates the density of the field-line tracings in the SOL. Along each field line shown in Figures 4.3-4 and 4.4-3, the magnetic field parallel to a field line in the equatorial plane (consisting of a radial component, B_R, and a toroidal component, B_ϕ), the magnetic field perpendicular to the equatorial plane (equivalently, the vertical field, B_V), and the flux-surface expansion factor are tabulated for input to the target-design task (Section 11.4). Results for a few representative lines are shown in Figures 4.4-4 and 4.4-5. The magnetic fields and the expansion factor are uniform far from the divertor (*i.e.*, $L = 0$), with the inboard fields being larger than the outboard fields because of toroidal effects. The separatrix is bracketed tightly by the field-line tracings at $r = 0.5995$ and $0.6005\ m$, so that the dotted lines in Figures 4.4-4 and 4.4-5 are superimposed upon the solid lines in the plasma chamber until these lines separate in the vicinity of the null where the toroidal field is a minimum and the expansion factor is a maximum. As the field lines proceed around the back of the nulling coil and actually intercept the coil on the inboard side, the parallel field reaches its maximum value at the same location where the perpendicular field and expansion factor are a minimum. The inverse minor-radius dependence of the perpendicular field and the inverse major-radius dependence of the parallel field are demonstrated between the results at the separatrix ($r = 0.6005\,\mathrm{m}$) and at the first wall ($r = 0.6600\,\mathrm{m}$). Although flux-surface expansion factors much larger than two occur along the field line adjacent to the separatrix, the collector plate cannot be positioned at those locations because of the required four neutral-mean-free-path buffer

Table 4.4-II.

DF-COIL PARAMETERS FOR TITAN-I AND -II

	TITAN-I[a]			TITAN-II[b] (Intermediate)		TITAN-II[b] (Final)	
	Nulling	Flanking	Trim	Nulling	Flanking	Nulling	Flanking
Number per trisector	1	2	2	1	2	1	2
Toroidal angle (^{o})	0	5.717	2.935	0	5.729	0	4.011
Major radius (m)	3.946	3.945	3.9	3.962	3.945	3.963	3.940
Minor radius (m)	0.855	0.860	0.900	0.846	0.850	0.879	0.830
Current per coil (kA)	164.00	82.00	131.07	162.50	81.25	280.00	140.00
Current density[c] (MA/m^2)	20[d]	20[d]	15[d]	25	25	50	25
Average current density (MA/m^2)	27.532[e]	29.095[e]	20.835[e]	25	25	50	25
Resistivity, $\eta(\mu\Omega\ m)$	0.35313	0.35313	0.35313	0.020	0.020	0.020	0.020
Power per coil (MW)	11.754	6.238	7.382	0.617	0.310	2.209	0.522
Conductor volume ($10^{-2}m^3$)	3.2001	1.5229	3.5574	2.419	1.215	2.165	2.044
Coil volume ($10^{-2}m^3$)	3.6206	1.8189	4.0147	3.456	1.736	3.093	2.920
Total average current density (MA/m^2)		25.1		25		35.7	
Conductor filling fraction, λ		0.874		0.7		0.7	
Steady-state dissipated power(MW)		116.980		3.711		9.757	
Inboard/outboard/average values at $r = 0.6005\ m$							
Watershed-to-null distance, $L_N(m)$		53.9/91.4/72.7		50.7/86.0/68.3		53.5/88.3/70.9	
Watershed-to-plate distance, $L_P(m)$ [f]		55.2/94.0/74.6		52.1/88.0/70.0		55.9/91.6/73.8	
Peak flux-surface expansion factor[f]		2.27/4.23/3.25		2.47/4.25/3.36		3.07/5.14/4.11	

[a] Design plasma-surface field values: $B_{\phi R} = 0.36\ T$ and $B_\theta(r_p) = 5.6\ T$.

[b] Design plasma-surface field values: $B_{\phi R} = 0.38\ T$ and $B_\theta(r_p) = 5.91\ T$.

[c] Outboard equatorial-plane value.

[d] Current density obtained by averaging current over conductor and structure.

[e] Includes effect of variable coil cross section and constant structural cross-sectional area associated with 2.5-mm-thick walls.

[f] Values are measured at 22.1 mm from the null.

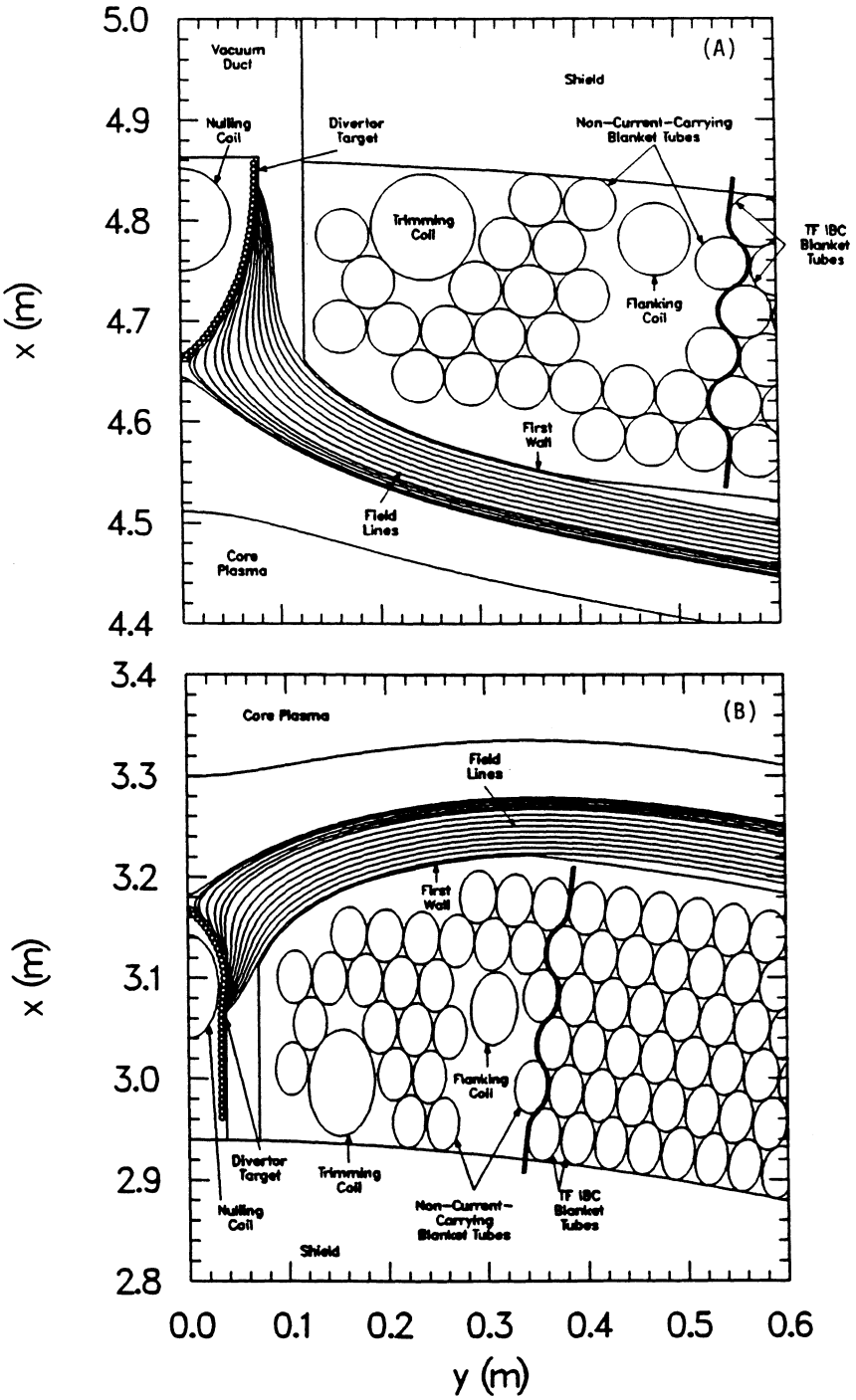

Figure 4.4-3. An expanded view of the TITAN-I divertor configuration outboard (A) and inboard (B) shown in Figure 4.3-4 and described in Table 4.4-II. The field lines are at r = 0.5449, 0.5995, 0.6005, 0.6010, 0.6030, 0.6060, 0.6090, 0.6120, 0.6180, 0.6240, 0.6300, 0.6360, 0.6420, 0.6480, 0.6540, and 0.6600 m.

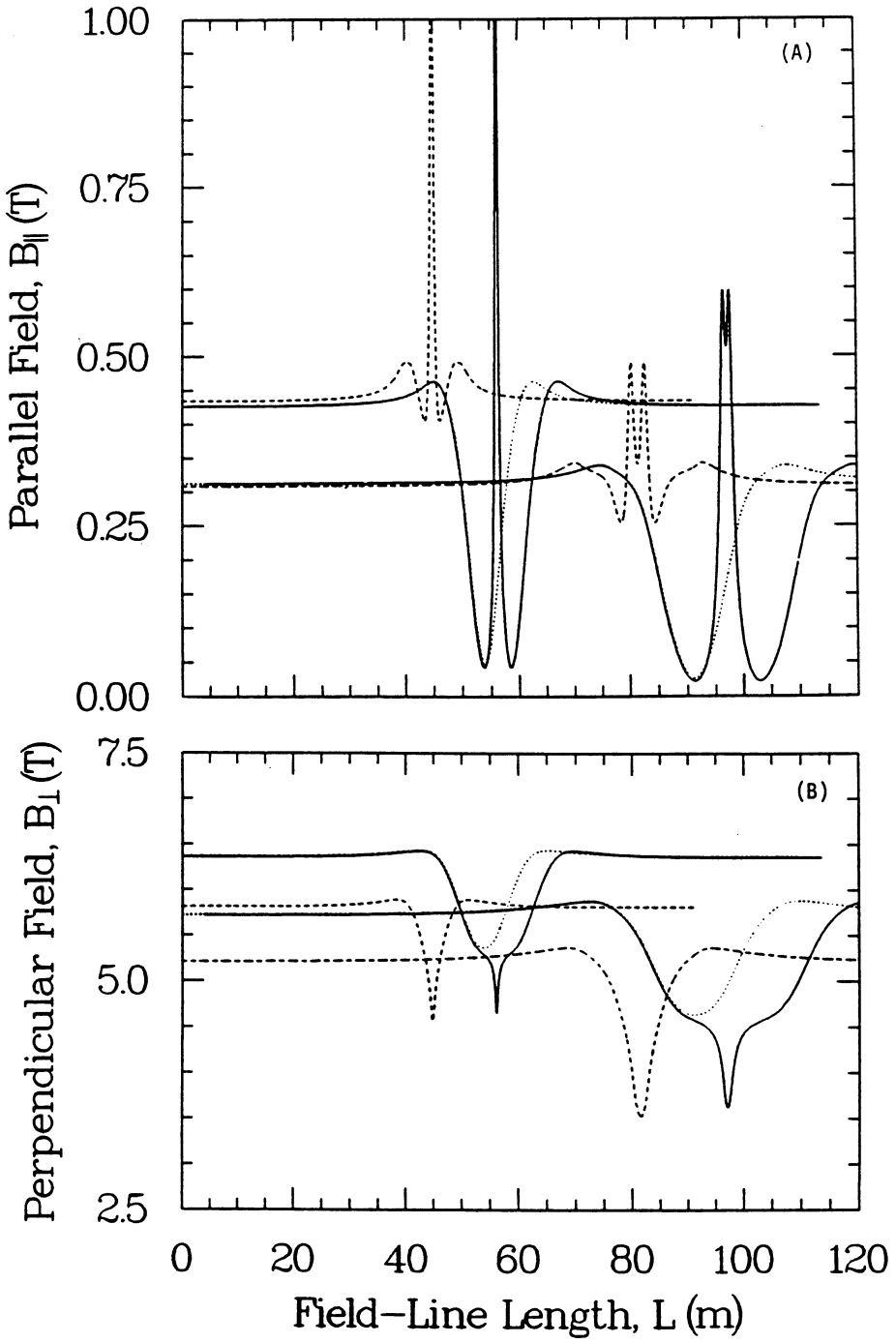

Figure 4.4-4. Parallel (A) and perpendicular (B) magnetic-field strength along the field line with length measured from the divertor midplane for TITAN-I. The fields correspond to field lines at $r = 0.5995$ (dotted line), 0.6005 (solid line), and 0.6600 m (dashed line) both inboard (higher initial field values) and outboard.

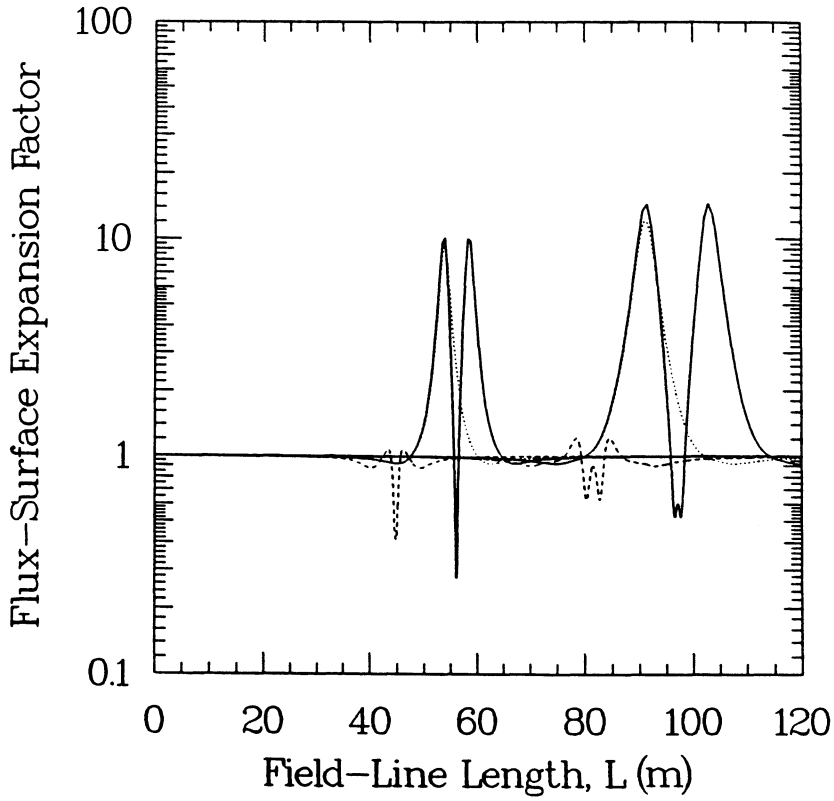

Figure 4.4-5. Flux-surface expansion factor along the field line with the length measured from the divertor midplane for TITAN-I. The expansion factors correspond to field lines at $r = 0.5995$ (dotted line), 0.6005 (solid line), and 0.6600 m (dashed line) both inboard (curves with spikes between 40 and 70 m) and outboard.

zone between the divertor plate and the null. This buffer zone is needed to attenuate the neutral flux before they can enter the plasma.

4.4.3. TITAN-II DF-Coil Design

Since TITAN-I and TITAN-II have similar blanket thicknesses (~ 0.28 m), the divertor design for TITAN-II was initiated with a simple conversion of the TITAN-I design into the intermediate TITAN-II divertor design presented in Table 4.4-II. The similarity of these two designs in all respects except the conductor (*i.e.*, Li versus Cu alloy) permits a precise documentation of the impact of the two conductors on overall performance. The difference in resistivity accounts for a factor of 0.06 reduction in the ohmic dissipation from TITAN-I to the intermediate TITAN-II design. A factor of 0.7 from TITAN-I to

the intermediate TITAN-II is attributable to the IBC being a single-turn coil, in which the ohmic losses in the two meters of leads cannot be ignored, as is the case for multi-turn Cu-alloy coils. Another factor of 0.6 results from the requirement that the DF coils include a trim coil for the IBC design.

This intermediate TITAN-II design, however, requires a target design with a critical heat-flux limit which in turn requires a higher (~ 3) flux-surface expansion factor. The divertor design which meets the various constraints is shown in Figure 4.4-6 and described in Table 4.4-II. The design constraints were met by returning to the 4° spread between the nulling and flanking coils required to ensure acceptable magnetic islands. In addition, the nulling-coil minor radius and current were increased to achieve an expansion factor of ~ 3 within the constraint of an ohmic dissipation of $\leq 10\,\mathrm{MW}$. A maximum of 20 to 50 mm of shielding is possible inboard; this shield thickness increases to $> 100\,\mathrm{mm}$ outboard, as is shown in the expanded view of the divertor region in Figure 4.4-7. A maximum of 120 mm of shielding is possible for the flanking coils. Shielding is not necessary, however, to protect the insulators (Section 10.2), but shielding is desirable for purposes of energy recovery.

Plots of the parallel and perpendicular magnetic fields and the flux-surface expansion factor along the field line are shown in Figures 4.4-8 and 4.4-9. These three plots are similar to the TITAN-I plots of Figures 4.4-4 and 4.4-5 with the exception of the effect of TF ripple. The field-line tracings begin in the divertor midplane, which is midway between TF coils where the toroidal field is a minimum. Because the opening between TF coils is larger at the outboard than at the inboard position, the ripple is larger for the outboard field lines. Furthermore, a ripple is observed in the perpendicular or poloidal field because the radial excursions of the toroidal field lines result in minor-radius variations, which in turn affect the magnitude of the poloidal field. The ripple of both components of the magnetic field in the SOL could result in a weak mirror trapping of particles and enhance radial diffusion to the first wall. For the purposes of edge-plasma modeling, however, field ripple is neglected.

4.5. OHMIC-HEATING (OH) COILS

4.5.1. Models and Constraints

The single-turn back-bias and forward-bias OH-coil currents (respectively, I_{OH}^{-} and I_{OH}^{+}) are determined by the inductive-flux conservation, and ignoring the resistive losses:

$$L_p\, I_\phi \;=\; M_{EF,p}\, I_{EF} + M_{OH,p}\,(I_{OH}^{+} - I_{OH}^{-})\,, \qquad (4.5\text{-}1)$$

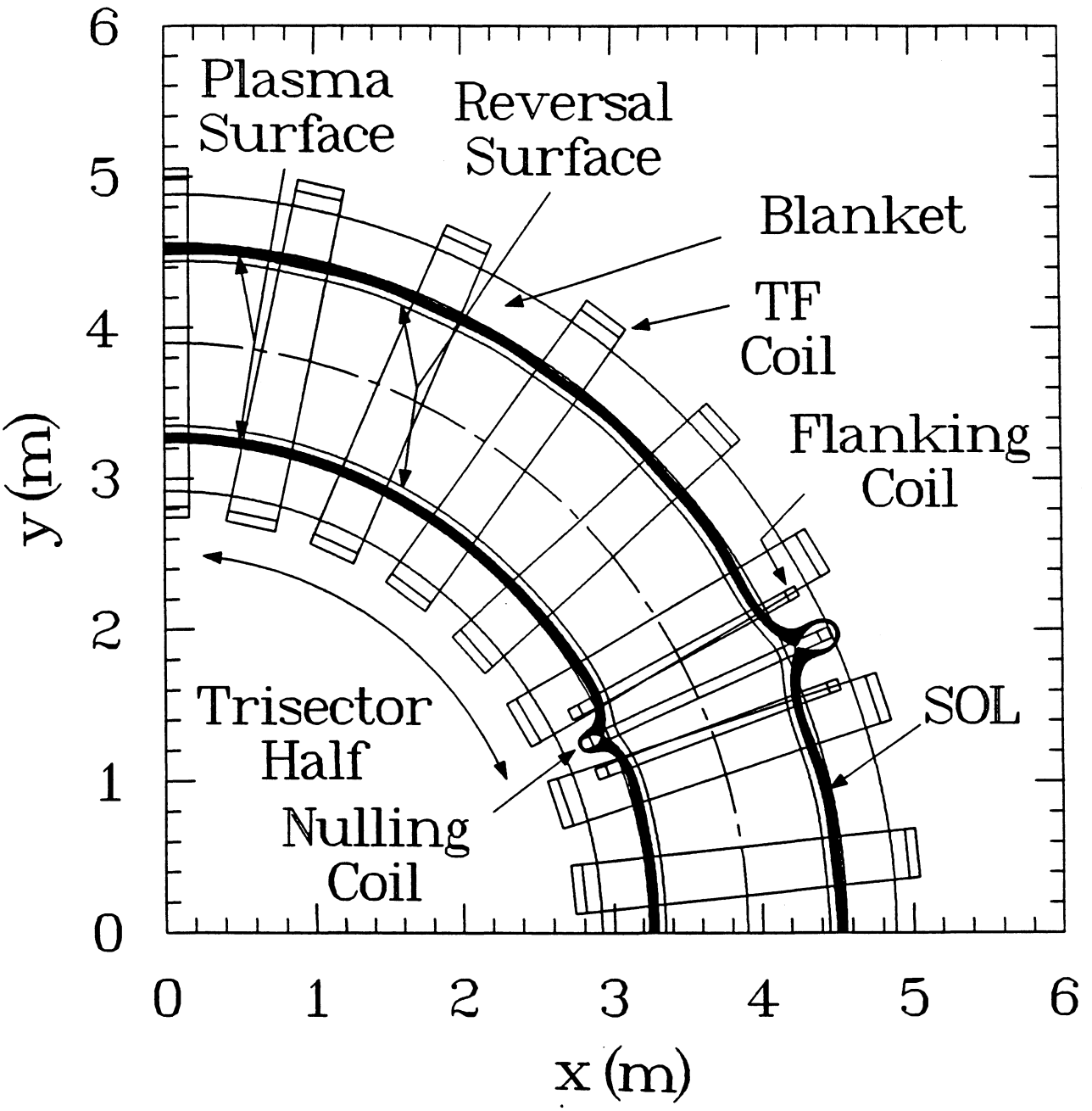

Figure 4.4-6. Equatorial-plane view of TITAN-II divertor design. Also shown are field-line tracings at inboard and outboard minor radii of $r = 0.5494$, 0.5995, 0.6005, 0.6010, 0.6030, 0.6060, 0.6090, 0.6120, 0.6180, 0.6240, 0.6300, 0.6360, 0.6420, 0.6480, 0.6540, and 0.6600 m.

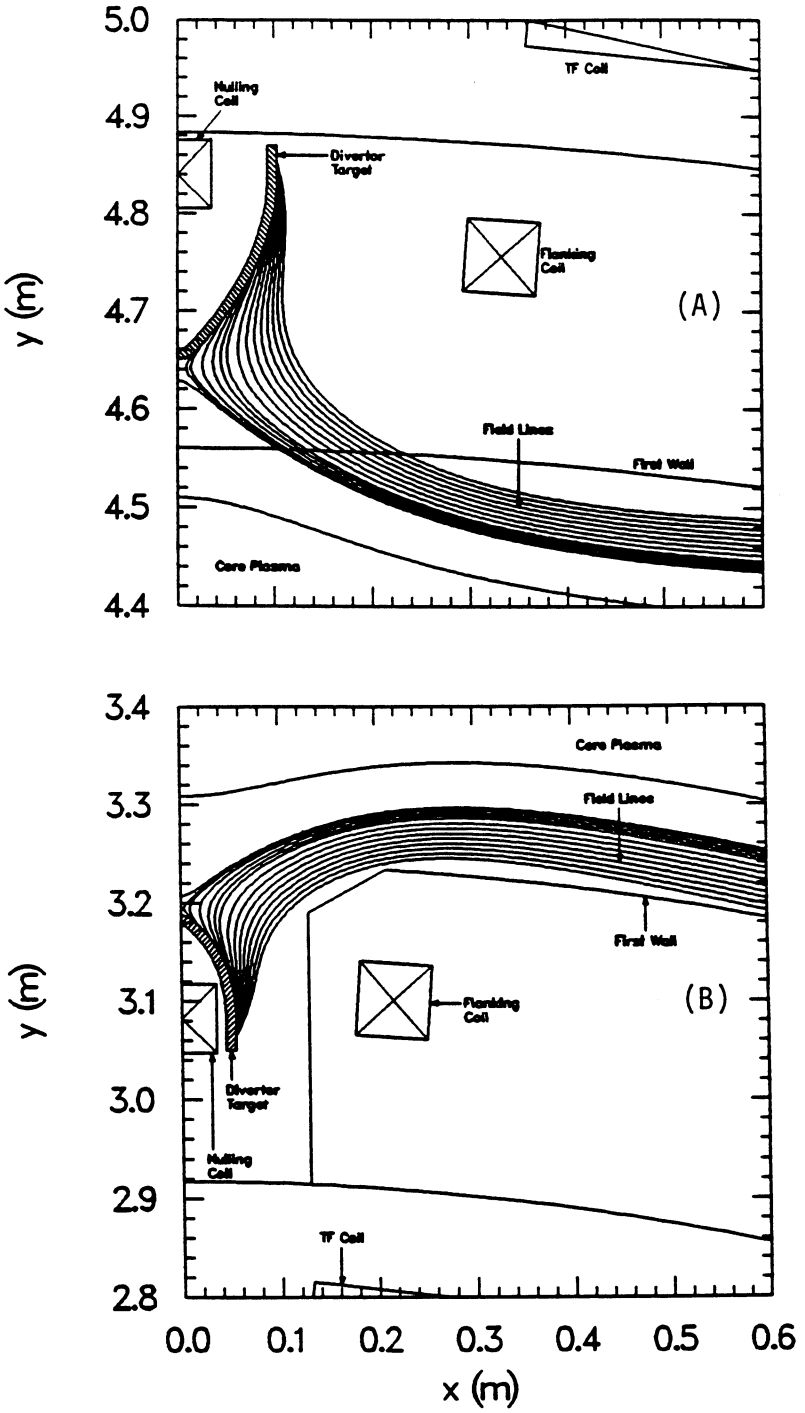

Figure 4.4-7. An expanded view of the TITAN-II divertor configuration outboard (A) and inboard (B) shown in Figure 4.4-6 and described in Table 4.4-II. The field lines are at $r = 0.5494$, 0.5995, 0.6005, 0.6010, 0.6030, 0.6060, 0.6090, 0.6120, 0.6180, 0.6240, 0.6300, 0.6360, 0.6420, 0.6480, 0.6450, and 0.6600 m.

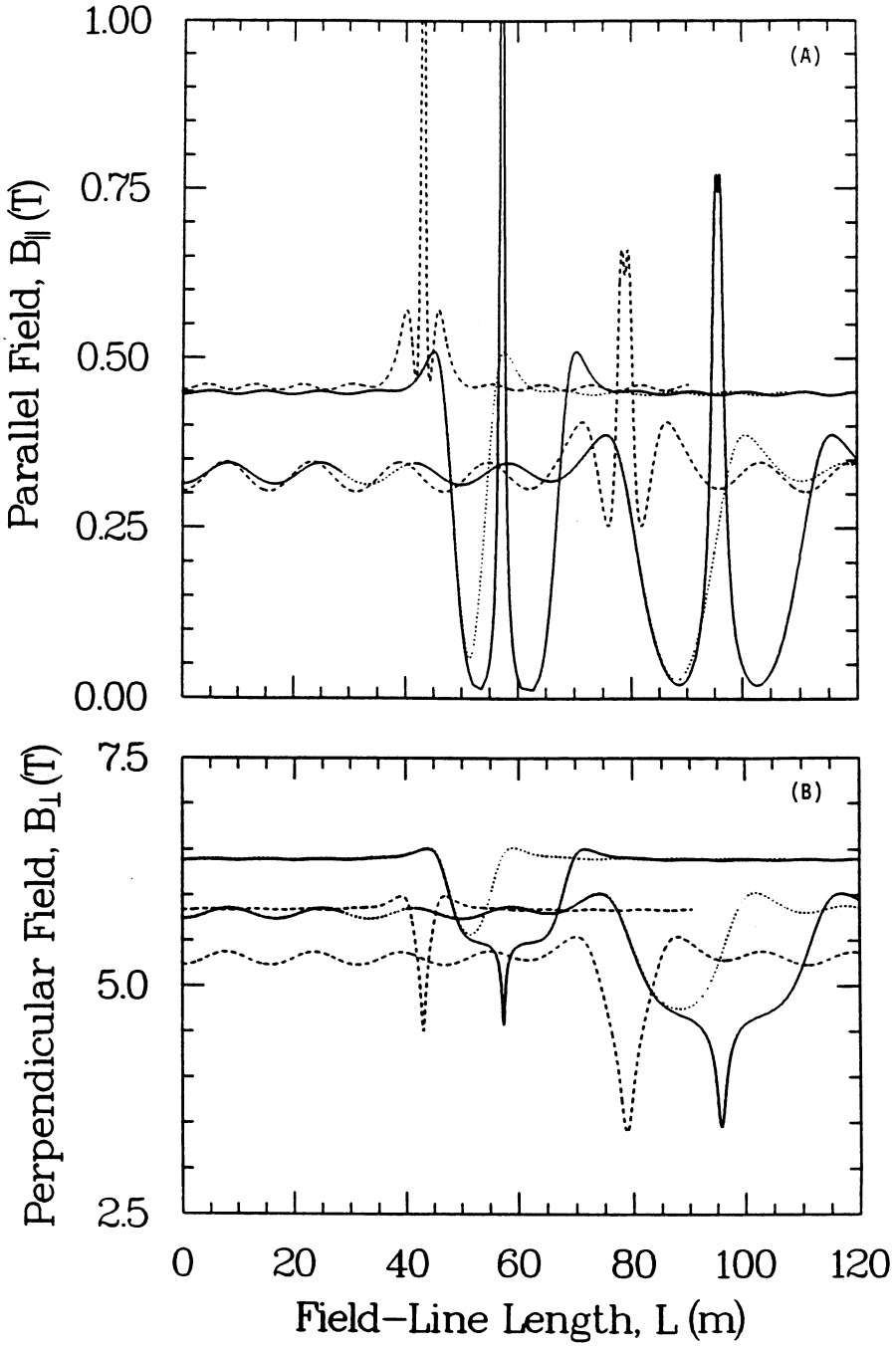

Figure 4.4-8. Parallel (A) and perpendicular (B) magnetic-field strength along the field line with length measured from the divertor midplane for TITAN-II. The fields correspond to field lines at $r = 0.5995$ (dotted line), 0.6005 (solid line), and 0.6600 m (dashed line) both inboard (higher initial field values) and outboard.

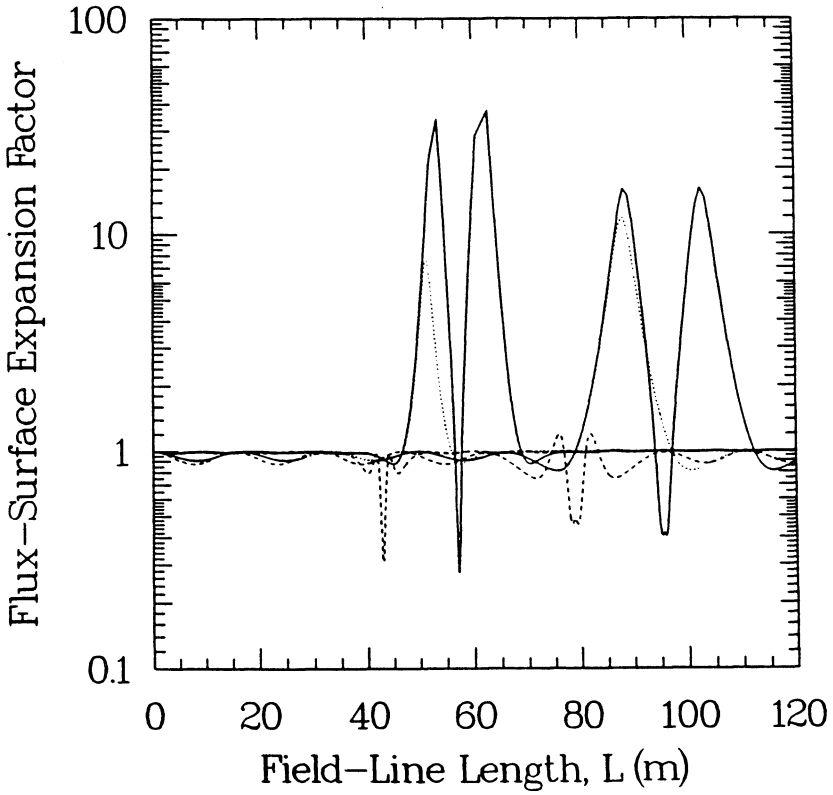

Figure 4.4-9. Flux-surface expansion factor along the field line with the length measured from the divertor midplane for TITAN-II. The expansion factors correspond to field lines at $r = 0.5995$ (dotted line), 0.6005 (solid line), and 0.6600 m (dashed line) both inboard (curves with spikes between 40 and 70 m) and outboard.

where I_ϕ and I_{EF} are the steady-state plasma and EF-coil currents, respectively, $M_{i,j}$ is the mutual inductance between the i^{th} and j^{th} circuit elements, and L_p is the plasma self-inductance. The parameter $f_G \equiv I_{OH}^+ / \mid (I_{OH}^- \mid$ is used to characterize the symmetry of the bipolar OH-current swing. For a symmetric bipolar swing, $f_G = 1$ while smaller values of f_G represent deeper initial back-bias current (*i.e.*, larger I_{OH}^-). The required OH-coil back-bias volt-seconds is

$$M_{OH,p}\, I_{OH}^- \;=\; \frac{L_p\, I_\phi - M_{EF,p}\, I_{EF}}{1 + f_G}\,. \tag{4.5-2}$$

The scoping analysis of the various OH-coil configurations for TITAN-I (Section 4.5.2) uses the code, CCOIL [2,17]. The locations of the OH coils are determined using CCOIL by first specifying an arc upon which the coils are to be arrayed; this arc is defined as a

segment of an ellipse that is symmetric about the equatorial plane. The coefficients for a Fourier series representation of the current distribution on the arc that excludes flux from the entire plasma cross section are then determined. Assuming equal-current coils to facilitate series electrical connection of the coils, the current distribution is integrated along the arc to yield the OH-coil current-center locations. This integration process used to determine the OH-coil locations introduces an error of $\geq 20\,\mathrm{mT}$ in the stray vertical field within the plasma. A manual adjustment of the OH-coil locations is then required to achieve the desired level of stray vertical field. A modified version of CCOIL was used to analyze the vertical-stack configuration discussed in Section 4.5.2. The locations of the vertical-stack OH coils are taken to be uniformly spaced within a stack. The coils within a stack are of equal current. The current distribution between stacks is determined by requiring the coil set to exhibit an on-axis field null in order to facilitate breakdown and formation of the initial RFP (Section 6.2).

The computer code, CCOIL, estimates the mutual inductances used in Equation 4.5-1 from the following formula for two coaxial hoops [18]:

$$M_{i,j} = \frac{2\mu_o (r_i r_j)^{1/2}}{k} \left[\left(1 - \frac{k^2}{2} \right) K(k) - E(k) \right] , \tag{4.5-3}$$

where

$$k = \frac{4\, r_i\, r_j}{(r_i + r_j)^2 + \Delta_z^2} . \tag{4.5-4}$$

The radii of the i^{th} and j^{th} hoops are r_i and r_j, Δ_z is the distance between the two parallel coil planes, and $K(k)$ and $E(k)$ are the complete elliptic integrals of the first and second kinds, respectively. Each coil in a set is simulated by 100 hoops to ensure a high degree of accuracy, especially in computing coil self-inductances.

When the calculation of the single-turn mutual inductance involves a coil set, a summation is performed over each hoop in each coil in the set; for example,

$$M_{OH,j} = \sum_{i=1}^{n_{OH}} M_{i,j} , \tag{4.5-5}$$

where $n_{OH} = 100\, N_{OH}$ is the number of hoops used to simulate the number of OH coils, N_{OH}. The single-turn self-inductances of the coil sets are determined by application of the formula for mutual inductance with both summations over the same coil set as follows:

$$L_k = \sum_{i}^{n_k} \sum_{j}^{n_k} M_{i,j} , \tag{4.5-6}$$

where all of the filaments are equi-spaced and carry equal currents. The singular element $M_{i,i}$ is replaced with the following expression for the self-inductance of a wire of infinite minor radius [18]:

$$M_{i,i} = \mu_o R_i \left[\ln\left(\frac{8R_i}{\Delta}\right) - 1.75\right] , \tag{4.5-7}$$

where R_i is the major radius of the hoop used to simulate a coil and Δ is the separation between the filaments and assumed to be 0.01 m.

For the final TITAN-I OH-coil design as well as that of TITAN-II, a new computer code is developed which allows a higher degree of flexibility in coil design. In these designs, the current densities in all coils are kept uniform and currents in OH coils are allowed to vary such that the number of turns in each coil remains an integer. The coil currents and locations are determined by matching the magnetic flux produced by the OH-coil, ψ, on the outermost flux surface to $\psi_o = M_{OH,p} I_{OH}^-$, as prescribed by Equation 4.5-2. For TITAN designs, the outermost flux surface is a circle with minor radius of $r_p = 0.6$ m. This magnetic-flux matching is performed by a numerical optimizer routine which minimizes the functional

$$F = \sum_{S=1}^{N_S} \left[1 - \frac{\psi(\mathbf{r_s})}{\psi_o(\mathbf{r_s})}\right]^2 , \tag{4.5-8}$$

where N_S points on the matching flux surface are chosen, each located at position $\mathbf{r_s}$. Because of the up-down symmetry of the TITAN designs, only points on the upper half of the flux surface (above equatorial plane) are considered. The number of points N_S is usually set at a prime number to ensure that resonant multi-poles would not result in a false matching. For initial calculations, $N_S = 23$ is used and the final design is checked with $N_S = 53$ points.

The components of the magnetic field and the vector potential are found by direct integration of the Ampere's law over the coil cross section. Using a cylindrical coordinates system $(RZ\theta)$ with Z axis lying on the axis of the torus and noting the toroidal symmetry, only one component of the vector potential is non-zero. For a circular coil with a rectangular cross section and the coil axis lying on the Z axis, the resulting vector potential at point (R, Z) is

$$A_\theta(R,Z) = \frac{\mu_o J}{2\pi} \int_o^\pi cos\theta \, d\theta \int_{Z_i - Z}^{Z_o - Z} dZ' \int_{R_i}^{R_o} \frac{R' \, dR'}{\left(Z'^2 + R^2 + R'^2 - 2RR'cos\theta\right)^{1/2}} , \tag{4.5-9}$$

where R_i and R_o are inner and outer coil radii and Z_i and Z_o are the heights of the bottom and top of the coil, respectively. The magnetic flux, ψ, can be directly calculated

from

$$\psi \equiv R A_\theta , \tag{4.5-10}$$

and the components of the magnetic field are given by

$$B_R = -\frac{\partial A_\theta}{\partial Z} , \tag{4.5-11}$$

$$B_Z = \frac{A_\theta}{R} + \frac{\partial A_\theta}{\partial R} . \tag{4.5-12}$$

Equation 4.5-9 is substituted in the above equations, resulting in similar 3-D integrals for B_R and B_Z.

Approximating each coil by a set of filaments is equivalent to carrying out the θ integration in Equation 4.5-9 analytically and using "mid-point" rules for R' and Z' integrals. As a result, the filamentary approximation requires a large number of filaments and will be inaccurate inside or near the coil because of the denominator of the integrand in Equation 4.5-9. For final TITAN-I design as well the TITAN-II OH-coil design, a different technique is used. The R' and Z' integrals in Equation 4.5-9, and similar equations for B_R and B_Z, are solved analytically and the integral over θ is evaluated numerically using an adaptive quadrature routine [19]. Similarly, the expression for mutual inductance of two coaxial circular coils with rectangular cross sections and the self-inductance of such coils can be written as 6-D integrals over the coils cross section. These 6-D integrals can be reduced analytically to 2-D integrals which are then evaluated numerically using adaptive quadratures [19].

Both the CCOIL computer code and the final TITAN OH-coil designs simulate the plasma as a single-hoop current that is positioned in the equatorial plane at a major radius, R_T^*, which includes a Shafranov shift [3]:

$$R_T^* = R_T + \frac{r_w^2}{2R_T}\left[\left(\beta_\theta + \frac{l_i}{2} - \frac{1}{2}\right)(1-x^2) - \ln x\right] , \tag{4.5-13}$$

where R_T is the torus major radius, r_w is the first-wall minor radius, and $x = r_p/r_w$ is the ratio of plasma and first-wall minor radii. This is a good approximation for circular plasmas with high aspect ratios.

The plasma self-inductance is expressed as a sum of an external inductance, $L_{p,ex}$, and an internal inductance, $L_{p,in}$, (*i.e.*, $L_p = L_{p,in} + L_{p,ex}$). The external inductance is taken to be that for a wire with the same dimensions as the plasma [18]

$$L_{p,ex} = \mu_o R_T \left[\ln\left(\frac{8R_T}{r_p}\right) - 2\right] . \tag{4.5-14}$$

The internal inductance is derived from a 1-D equilibrium calculation (Section 5.2) and is given by

$$L_{p,in} = \left[2\pi R_T (W_\theta + W_\phi) - \frac{\phi^2}{2L_o}\right] I_\phi^2 , \tag{4.5-15}$$

where

$$W_i \equiv \frac{\pi}{\mu_o} \int_0^{r_p} B_i^2(r)\, r dr , \tag{4.5-16}$$

$$\phi \equiv 2\pi \int_0^{r_p} B_\phi(r)\, r dr , \tag{4.5-17}$$

$$L_o \equiv \frac{\mu_o r_p^2}{2R_T} . \tag{4.5-18}$$

In addition to providing the adequate volt-seconds, the OH-coil design is constrained by the maximum level of the stray vertical field during breakdown (Section 6.2). This constraint specifies the stray vertical field produced by the OH-coil set as a fraction of the initial toroidal field, $B_{\phi o}$. In principle, the initial toroidal field, $B_{\phi o}$, can be increased to ensure compliance with the stray-vertical-field constraint. Any increase in $B_{\phi o}$, however, would result in increases in the OH-coil flux consumption as well as increases in the formation energy and power. A single order of magnitude increase in the value of $B_{\phi o}$ would result in a flux consumption during formation ≥ 80 V-s, a formation energy ≥ 200 MJ, and a formation power ≥ 1 GW (Section 6.2). Consequently, a maximum value of 2.45 mT for the stray vertical field is adopted. A secondary constraint is that the OH-coil set exhibit a field null within the plasma chamber. A field null provides a closed field line upon which to initiate a current channel. Finally, the PF-coil parameters listed in Table 4.1-I provide design guidance for the OH coils.

4.5.2. OH-Coil Configurations

The desire to optimize the OH-coil performance, as measured by the electrical coupling between the OH coil and the plasma, conflicts with design-integration requirements for access to the TF coils, blanket, and vacuum chamber. Other magnet engineering issues such as stresses, cooling requirements, and the magnet support structure should also be considered. Consequently, a search was conducted for an OH-coil configuration with both good access and performance properties. The OH-coil configurations surveyed are a "close-fitting" configuration (shown in Figure 4.5-1), and a "vertical stack" configuration and a range of "pill box" configurations (shown in Figures 4.5-2 and 4.5-3).

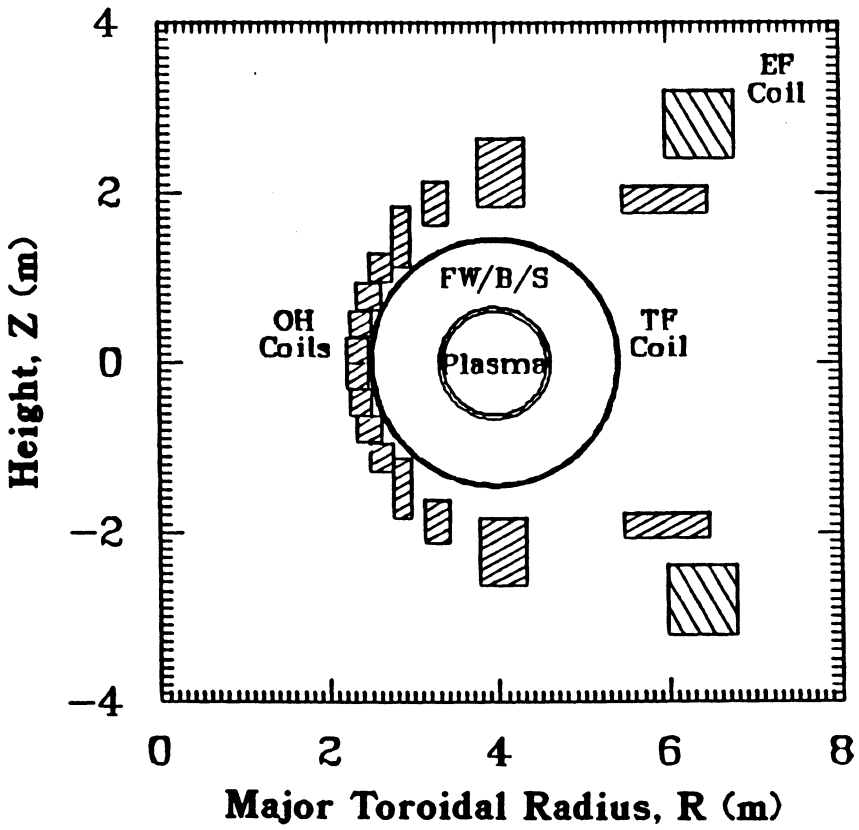

Figure 4.5-1. A "close-fitting" OH-coil configuration that maximizes the electrical coupling between the plasma and OH coils used in OH-coil configurational analysis.

The close-fitting configuration yields the best electrical coupling to the plasma, as is indicated by the mutual inductances between the OH coils and the plasma (Table 4.5-I); OH-coil transparency is sacrificed, however. The OH-coil transparency reported in Table 4.5-II is defined as the fraction of the equatorial-plane cross-sectional area of the torus bounded by the TF coils that is vertically unobstructed by OH coils. The transparency is maximized by the vertical-stack configuration. The vertical-stack configuration, however, violates by nearly two orders of magnitude the liberal stray-vertical-field constraint of $\leq 8\,\mathrm{mT}$ operative during this configurational study. Compliance with a stray-vertical-field constraint of a few mT requires the placement of OH coils over the torus. A compromise configuration between the close-fitting and vertical-stack configurations is the pill-box configuration. By varying the height of the pill-box configuration, the inductive coupling to the plasma approaches 93% of that for the close-fitting configuration, but the OH-coil transparency decreases below that of the close-fitting configuration.

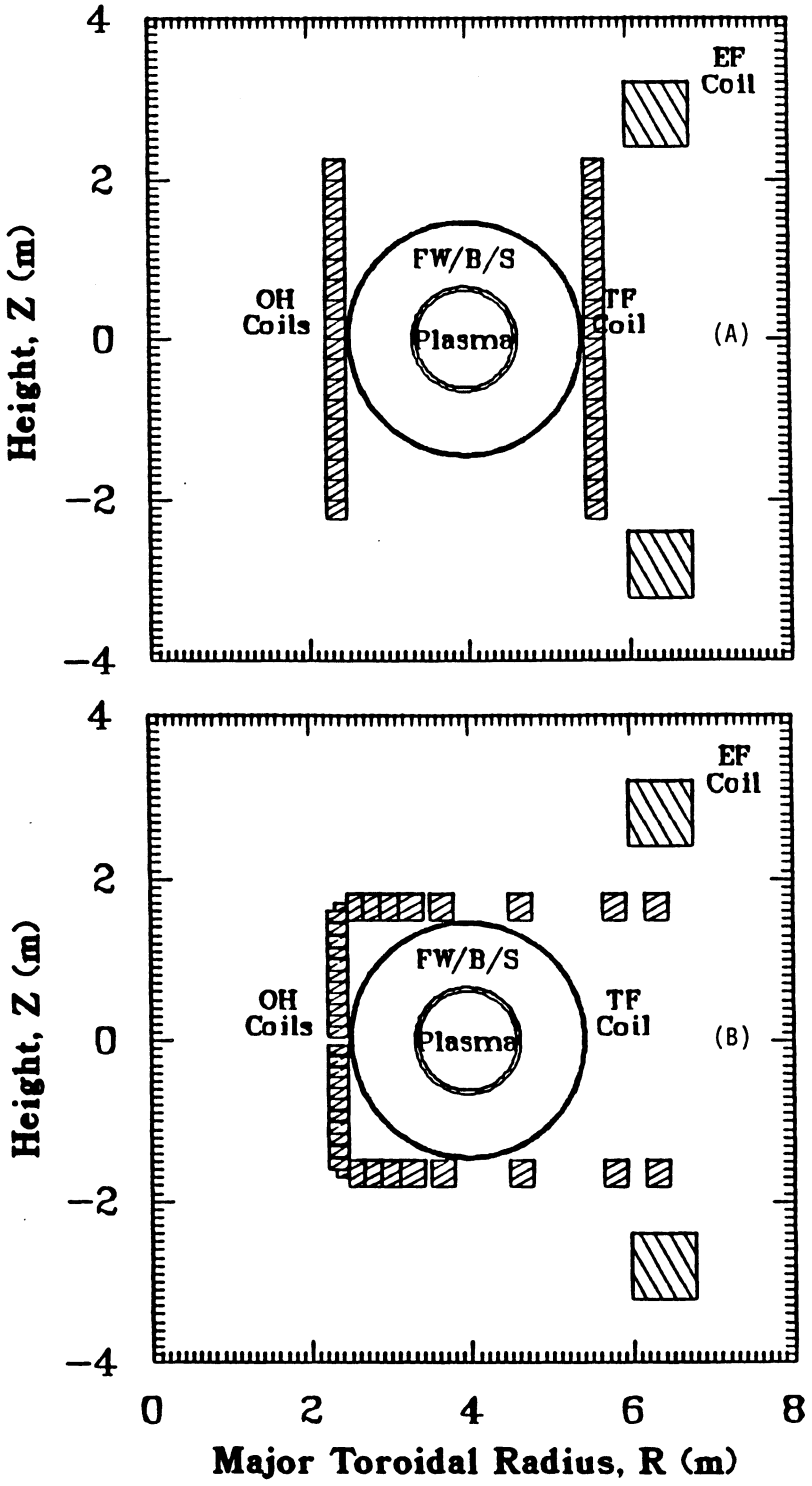

Figure 4.5-2. A "vertical-stack" configuration that maximizes the OH-coil transparency (A) and a "pill-box" configuration with a low vertical extent (B) used in OH-coil configurational analysis.

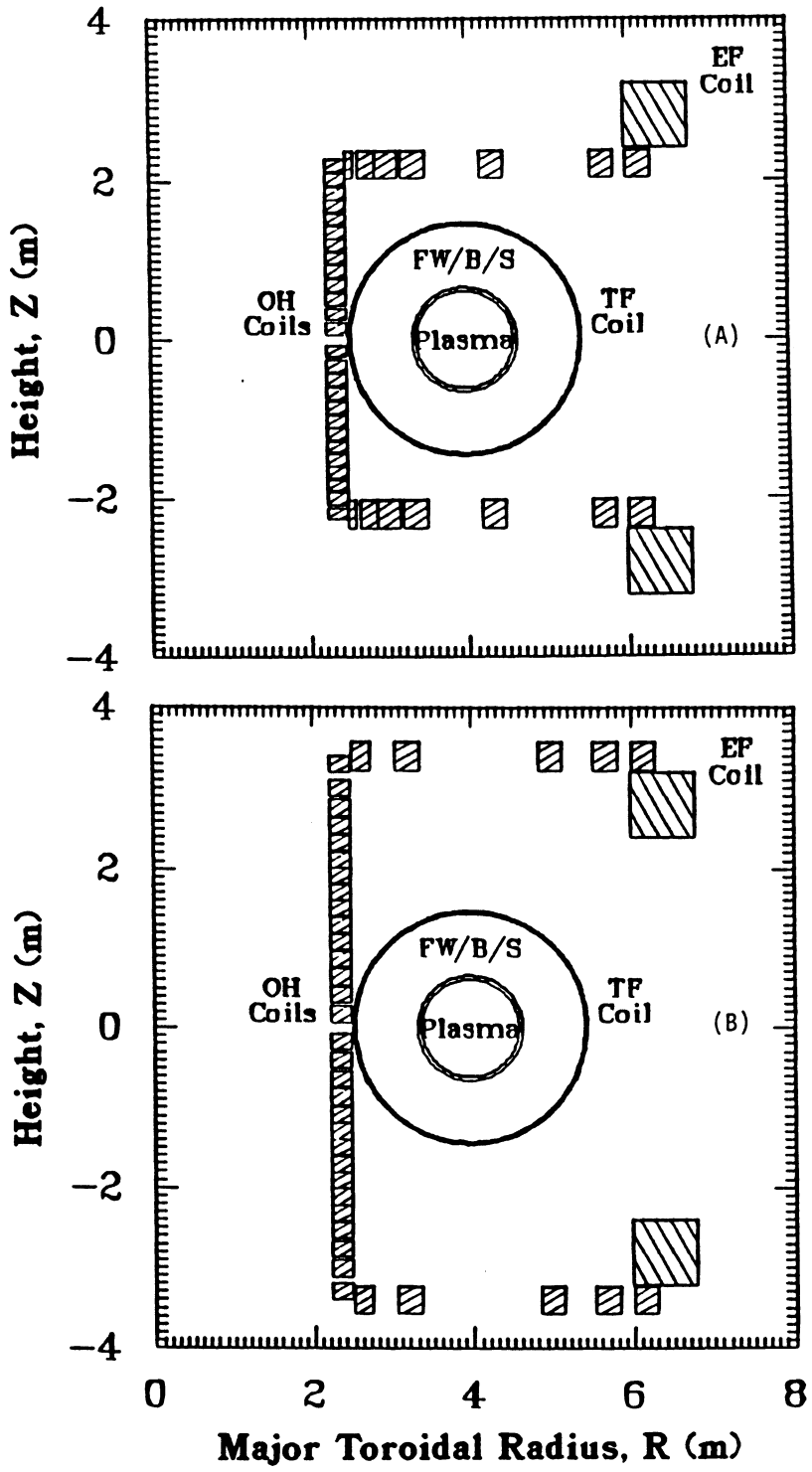

Figure 4.5-3. "Pill-box" configurations with a medium vertical extent (A) and a high vertical extent (B) used in OH-coil configurational analysis.

Table 4.5-I.

CIRCUIT PARAMETERS FOR TITAN-I OH-COIL CONFIGURATIONAL ANALYSIS

	Close Fitting	Vertical Stack	Pill Box		
			Low	Medium	High
Self inductances (μH)					
· L_p	13.5	13.5	13.5	13.5	13.5
· L_{EF}	29.1	29.1	29.1	29.1	29.1
· L_{OH}	4.31	3.32	3.46	2.98	2.41
Mutual inductances (μH)					
· $M_{OH,p}$	3.60	3.02	3.34	2.82	2.24
· $M_{OH,EF}$	3.01	2.12	2.54	2.52	2.44
· $M_{EF,p}$	3.72	3.72	3.72	3.72	3.72
Current levels (MA)					
· I_ϕ	21.7	21.7	21.7	21.7	21.7
· I_{EF}	23.2	23.2	23.2	23.2	23.2
· ΔI_{OH}	56.9	67.9	61.5	72.8	91.5
Magnetic fluxes (Wb)					
· Plasma	291.5	291.5	291.5	291.5	291.5
· EF coil	86.4	86.4	86.4	86.4	86.4
· OH coil	205.1	205.1	205.1	205.1	205.1

Table 4.5-II.

RESULTS OF TITAN-I OH-COIL CONFIGURATIONAL ANALYSIS

	Close Fitting	Vertical Stack	Pill Box		
			Low	Medium	High
OH-coil back-bias current (MA)	28.5	34.0	30.7	36.4	45.7
OH-coil volume (m^3)	66.1	60.5	49.4	47.9	52.2
OH-coil mass (tonne)	482.5	441.7	360.6	349.7	381.1
OH-coil joule losses (MW)	214.7	319.0	261.7	324.6	411.6
OH-coil von Mises stress (MPa)	198.6	113.2	135.9	124.0	127.8
OH-coil peak field (T)	7.5	5.7	6.1	5.8	5.9
OH-coil current density (MA/m^2)[(a)]	22.9	24.4	48.0	29.7	21.1
OH-coil stray vertical field (mT)	7.8	658.4	8.0	6.8	0.3
OH-coil transparency (%)	61.7	100.	55.6	65.9	73.8

(a) Maximum values.

The failure of the low-profile pill-box configuration to outperform the close-fitting configuration led to the adoption of the close-fitting configuration as the interim TITAN-I OH-coil design. The close-fitting TITAN-I OH-coil design is shown in Figure 4.5-4 and described in Table 4.5-III. The presence of a field null at the back bias is shown in Figure 4.5-5. Compliance with the 2.45-mT stray-vertical-field constraint was monitored only in the equatorial plane, as is shown in Figure 4.5-6. As a result, compliance with the stray-vertical-field constraint does not occur in a small region of the plasma cross section, as is shown in Figure 4.5-5; compliance can be obtained, however, with only small adjustments to the coil locations.

The final TITAN-I OH-coil design strives to combine the good features of the close-fitting and pill-box configurations as shown in Figure 4.5-7. The final design also incorporates the magnet engineering issues of the stresses, cooling, and magnet support structure. The vertical stack of the pill-box configuration is retained which allows the

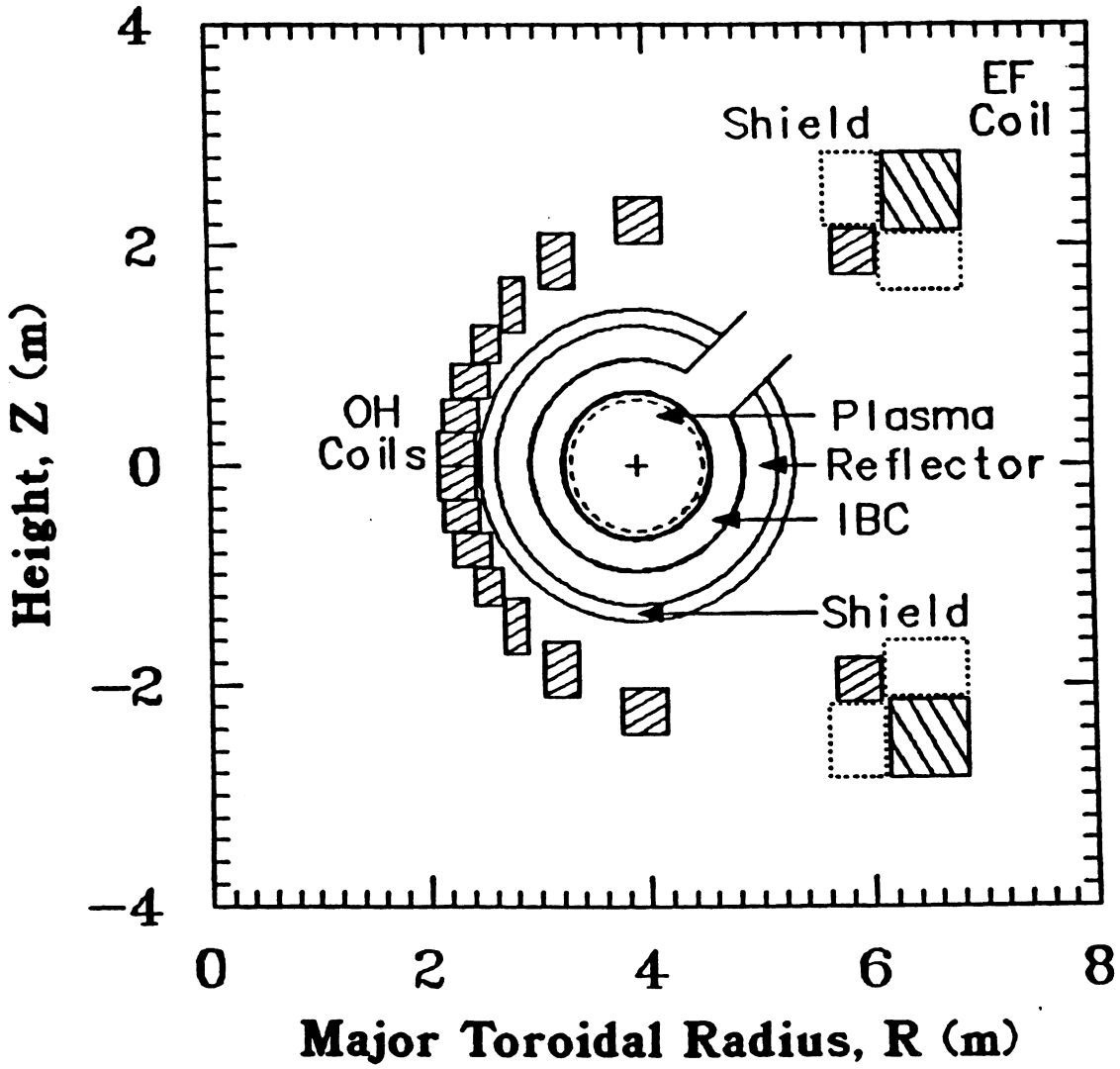

Figure 4.5-4. A cross-sectional view of the "close-fitting" OH-coil set for the intermediate TITAN-I design. The locations of the TF IBCs, the reflector, the shield, and the plasma are shown in addition to the EF coils and the OH coils.

Table 4.5-III.

PARAMETERS OF INTERIM TITAN-I POLOIDAL-FIELD COILS

Function	R (m)	$\pm z$ (m)	ΔR (m)	Δz (m)	$I^{(a)}$ (MA)	$j^{(a,b)}$ (MA/m^2)	Mass$^{(c)}$ (tonne)
Trim	5.7700	1.2000	0.2000	0.3000	0.	0.	15.9
EF	6.4959	2.4873	0.6973	0.6973	- 9.6189	19.78	144.9
OH-1	5.8699	1.9473	0.4000	0.4000	1.4556	9.10	43.1
OH-2	3.9472	2.2299	0.4100	0.4100	1.4556	8.66	30.4
OH-3	3.1958	1.8533	0.3000	0.5000	1.4556	9.70	22.0
OH-4	2.7905	1.4625	0.2000	0.5000	1.4556	14.56	12.8
OH-5	2.5503	1.1031	0.2500	0.3300	1.4556	17.64	9.7
OH-6	2.4028	0.7705	0.3300	0.3000	1.4556	14.70	10.9
OH-7	2.3163	0.4557	0.3200	0.3000	1.4556	15.16	10.2
OH-8	2.2759	0.1508	0.3300	0.3000	1.4556	14.70	10.3

(a) Mean steady-state values for the EF coils and back-bias values for the OH coils for a symmetric bipolar swing.

(b) Averaged over the entire coil cross section.

(c) A density of 7.3 tonne/m^3 is assumed.

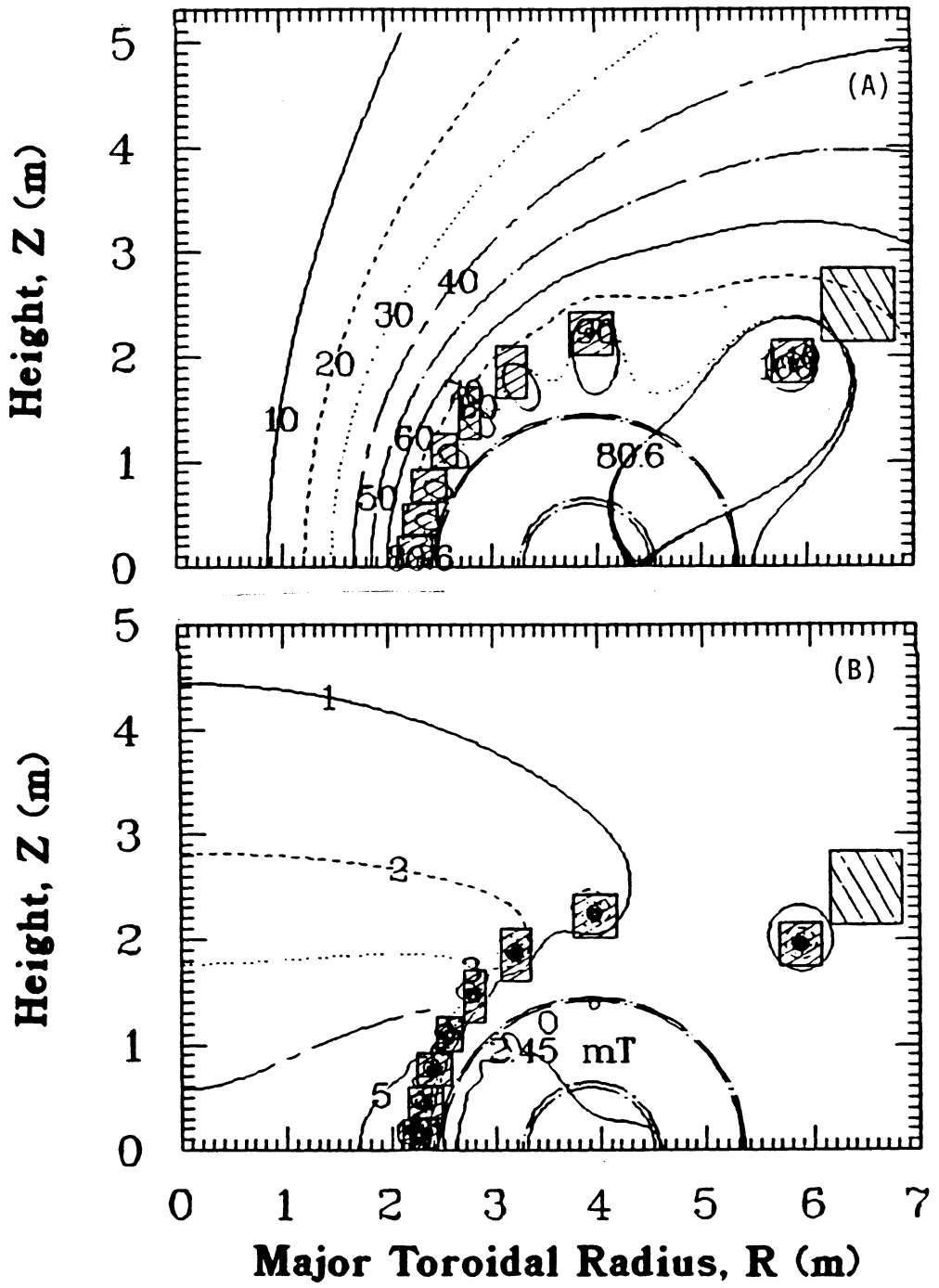

Figure 4.5-5. Contour plots of flux (A) and magnetic-field strength (B) for the intermediate TITAN-I OH-coil design. The flux contours, labeled in weber, demonstrate the presence of a field null within the plasma chamber. The magnetic-field contours are labeled in tesla, except the 2.45-mT contour which corresponds to the stray-vertical-field constraint.

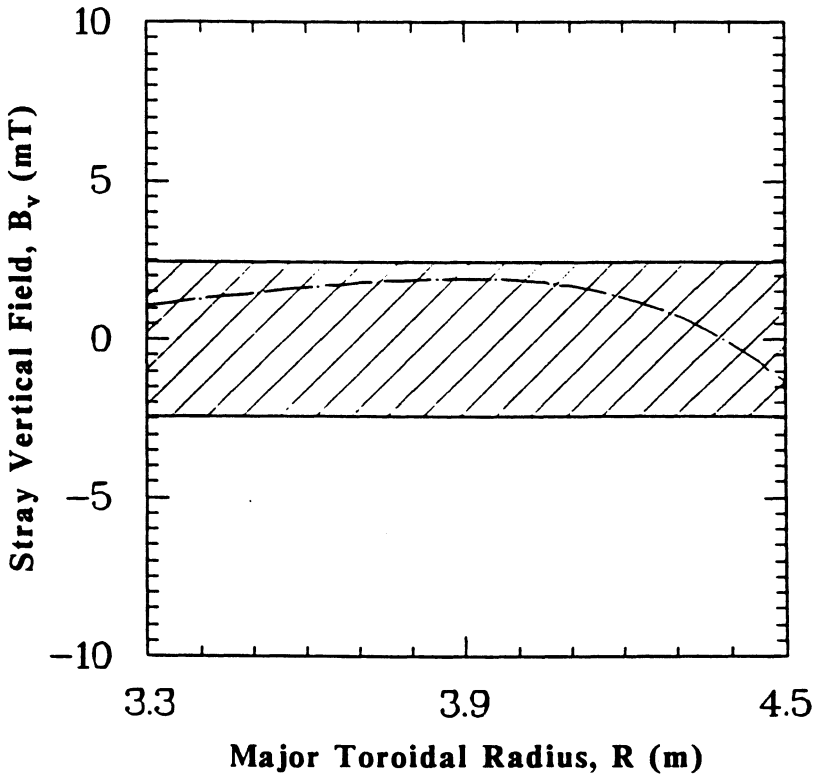

Figure 4.5-6. The stray vertical field for the intermediate TITAN-I OH-coil design in the equatorial plane. The hatched region represents the stray-vertical field constraint.

Lorentz forces from the upper coil set to be transmitted and canceled by the equal and opposite forces on the lower coil set. The coil OH-1 in Figure 4.5-7 is placed further away from the EF-coil set in order to reduce the forces on this coil during start-up transients. Coils OH-2 through OH-4 are arranged in a coil assembly which includes the support structure against bending moments produced by magnetic forces. During the maintenance operations, only the upper OH-coil assembly is removed; the vertical stack is installed permanently in the reactor vault. Detailed designs of the internal of the OH coils as well as the support structure are given in Section 10.5.

The final TITAN-I design is shown in Figure 4.5-7 and described in Tables 4.5-IV through 4.5-VI and compared with the parameters of the interim design. As expected, the intermediate design couples better to the plasma than the final design, which results in a 20% larger OH-coil current swing. But, the final design has the same coil mass and volume as the interim design, and lower peak joule heating and stresses. The stray vertical field produced by the final design is less than 0.5 mT in the entire plasma chamber.

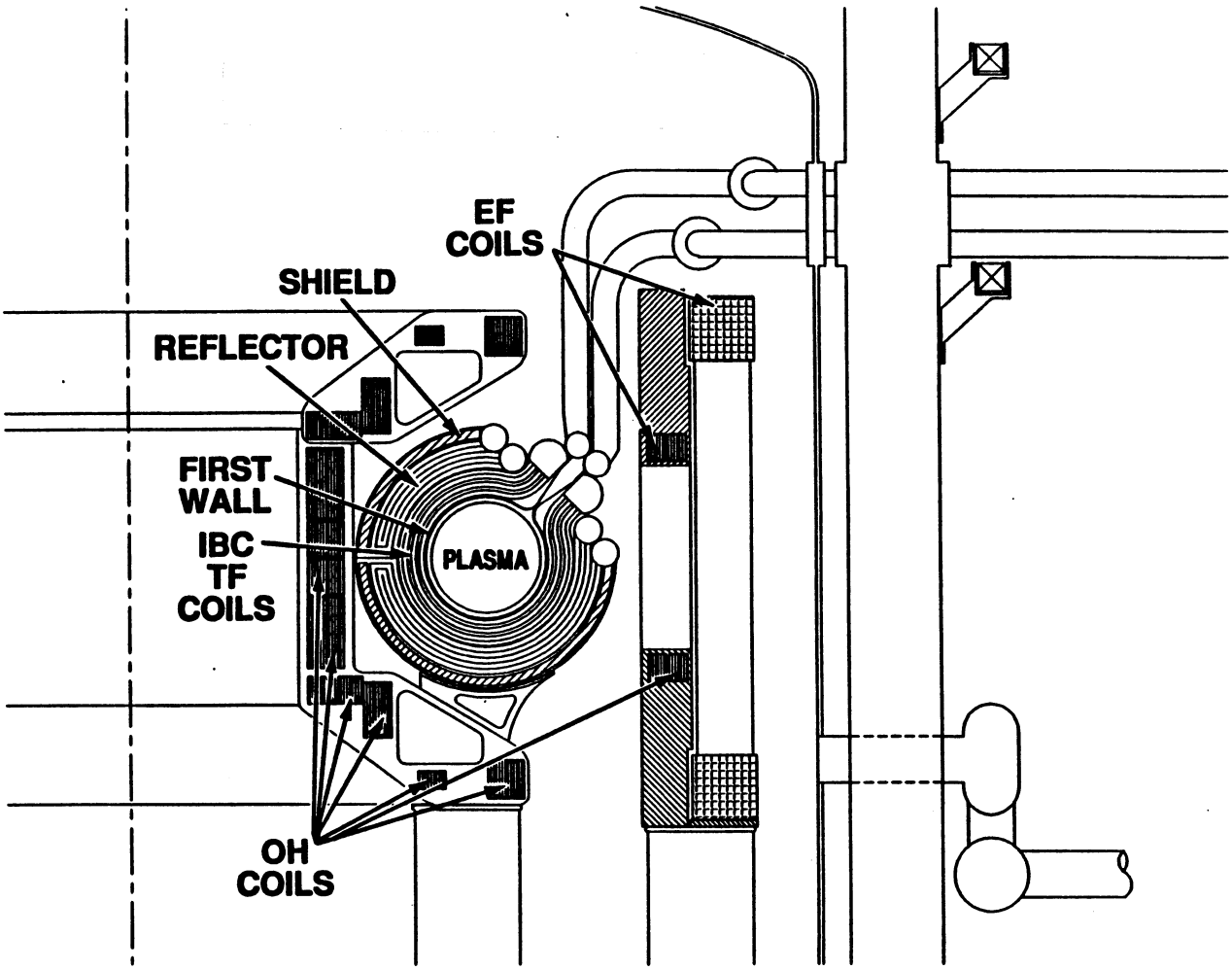

Figure 4.5-7. A cross-sectional view of the final TITAN-I OH-coil design. Also shown are the locations of the plasma, first wall, TF IBCs, reflector, shield, and EF coils.

The compliance of the final TITAN-I design with the constraints of a field null and the magnitude of the stray vertical field are demonstrated in Figure 4.5-8.

The TITAN-II OH-coil design shown in Figure 4.5-9 and described in Tables 4.5-VII through 4.5-IX is similar to the TITAN-I OH-coil design. The PF coils are closer to the plasma in TITAN-II, however, because of a thinner first wall, blanket, and shield (~ 0.45 m as opposed to ~ 0.75 m for TITAN-I) and the OH-coil mass is larger in TITAN-II as dictated by the parametric systems model of Section 3.2. The TITAN-II OH-coil design has the prerequisite field null and the stray vertical field complies with the 2.45-mT constraint, as is shown in Figure 4.5-9.

Table 4.5-IV.

PARAMETERS OF FINAL TITAN-I POLOIDAL-FIELD COILS

Coil	R (m)	$\pm z$ (m)	ΔR (m)	Δz (m)	$I^{(a)}$ (MA)	$j^{(a),(b)}$ (MA/m^2)	Mass$^{(c)}$ (tonne)	Turns
Trim	5.7700	1.2000	0.2000	0.3000	0.	0.	15.9	10
EF	6.4959	2.4873	0.6973	0.6973	- 9.6189	19.78	144.9	44
OH-1	6.0000	1.1963	0.2000	0.3000	0.7500	12.50	16.5	10
OH-2	4.1073	2.4050	0.4000	0.4200	2.1000	12.50	31.7	28
OH-3	3.2919	2.4000	0.3000	0.2000	0.7500	12.50	9.1	10
OH-4	2.7125	1.6538	0.3000	0.6000	2.2500	12.50	22.4	30
OH-5	2.2500	1.4307	0.6000	0.3000	2.2500	12.50	18.6	30
OH-6	2.1500	0.8100	0.4000	0.7800	3.9000	12.50	30.8	52
OH-7	2.1500	0.2050	0.4000	0.3900	1.9500	12.50	15.4	26

(a) Mean steady-state values for the EF coils and back-bias values for the OH coils for a symmetric bipolar swing.

(b) Averaged over the entire coil cross section.

(c) A density of 7.3 tonne/m^3 is assumed.

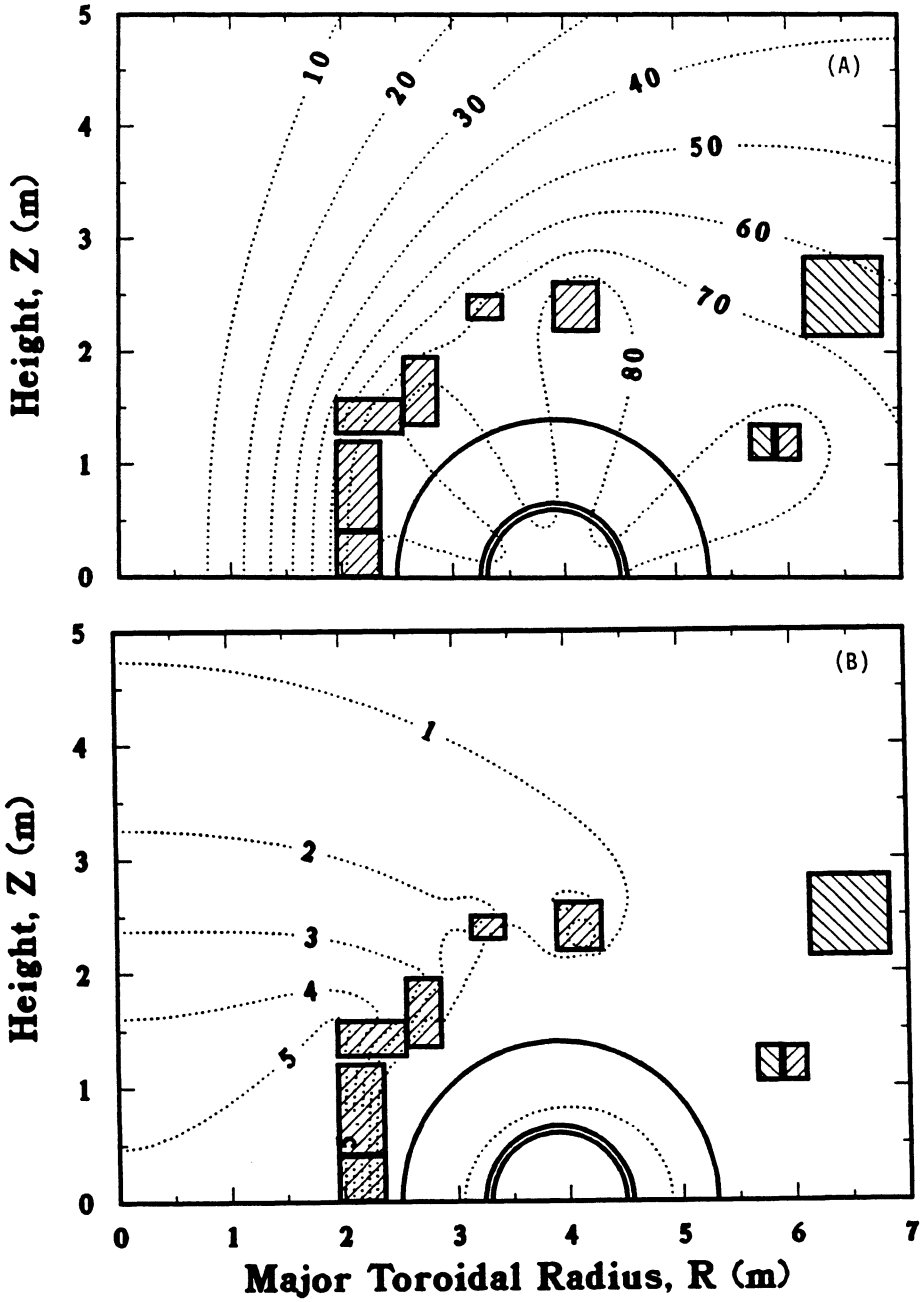

Figure 4.5-8. Contour plots of flux (A) and magnetic-field strength (B) for the final TITAN-I OH-coil design. The flux contours, labeled in weber, demonstrate the presence of a field null within the plasma chamber. The magnetic-field contours are labeled in tesla, except the 2.45-mT contour around the plasma chamber which corresponds to the stray-vertical-field constraint.

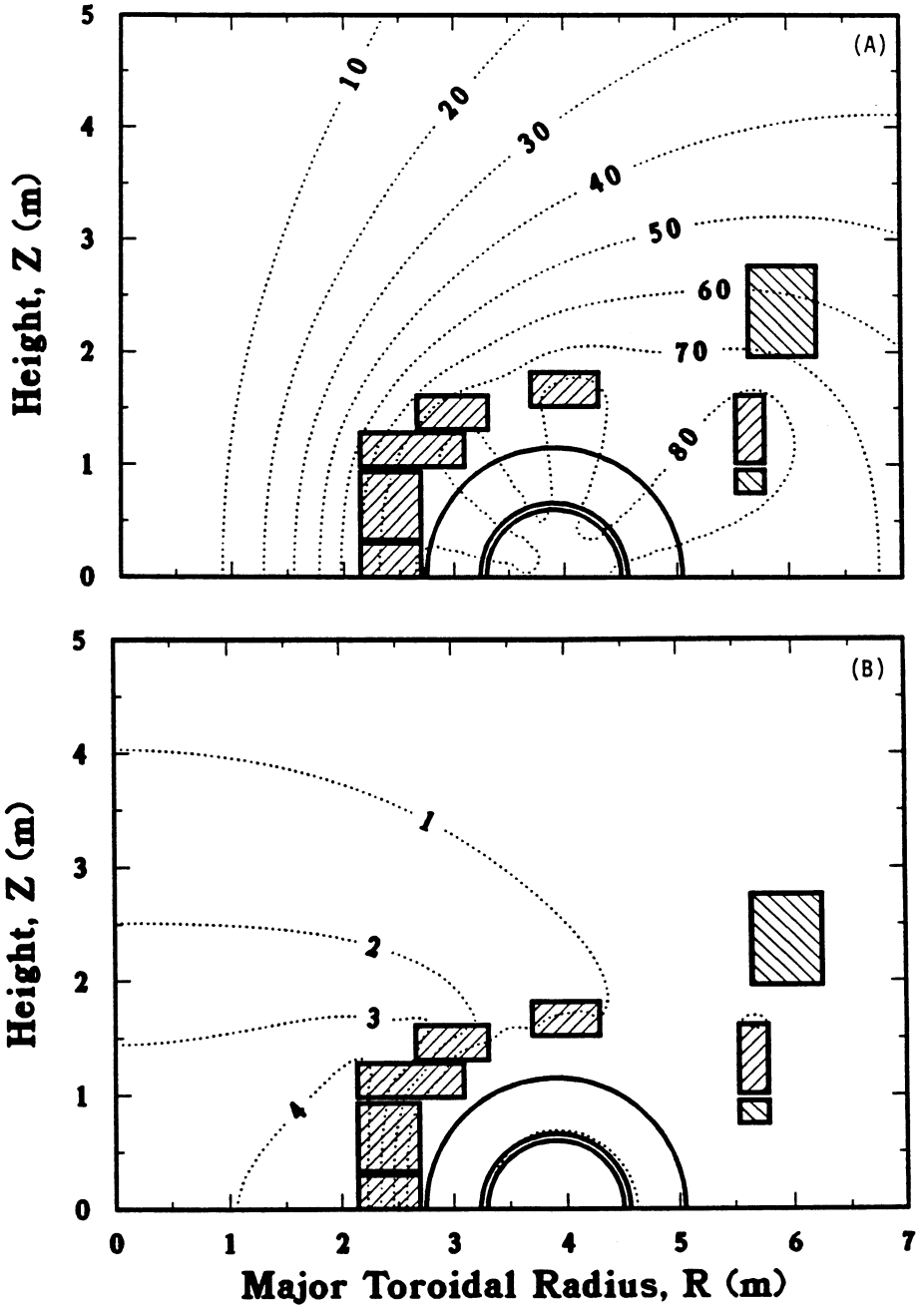

Figure 4.5-9. Contour plots of flux (A) and magnetic-field strength (B) for the TITAN-II OH-coil design. The flux contours, labeled in weber, demonstrate the presence of a field null within the plasma chamber. The magnetic-field contours are labeled in tesla, except the 2.45-mT contour around the plasma chamber which corresponds to the stray-vertical-field constraint.

Table 4.5-V.

CIRCUIT PARAMETERS FOR TITAN-I PF-COIL DESIGNS[a]

	Interim	Final
Self inductances (μH)		
· L_p	13.29	13.29
· L_{OH}	3.39	2.74
· L_{EF}	14.80	15.02
· L_{Trim}		18.36
Mutual inductances (μH)		
· $M_{OH,p}$	3.47	2.87
· $M_{OH,EF}$	3.08	2.26
· $M_{OH,Trim}$		2.99
· $M_{EF,p}$	3.88	3.86
· $M_{EF,Trim}$		8.69
· $M_{Trim,p}$		5.60
Current levels (MA-turn)		
· I_ϕ	17.75	17.75
· I_{EF}	19.24	19.24
· ΔI_{OH}	46.58	55.80
Magnetic fluxes (Wb)		
· Plasma	236.0	236.0
· EF coil	74.5	74.5
· OH coil	161.5	161.5

(*a*) Equivalent single-turn inductance values are given.

Table 4.5-VI.

PARAMETERS OF TITAN-I PF-COIL DESIGNS

	Interim	Final
EF-coil current (MA-turn)[a]	19.2	19.2
EF-coil volume (m^3)	39.7	39.7
EF-coil mass (tonne)	289.7	289.7
EF-coil peak field (T)[a]	6.4	6.4
EF-coil current density (MA/m^2)[a]	19.8	19.8
Vertical field index, n	0.16	0.16
OH-coil current (MA-turn)[b]	23.3	27.9
OH-coil volume	40.9	39.5
OH-coil mass (tonne)	298.8	288.4
OH-coil joule losses (MW)[b]	161.0	103.
OH-coil von Mises stress (MPa)[b]	100.9	89.
OH-coil peak field (T)[b]	5.9	5.7
OH-coil current density (MA/m^2)[b]	8.6 to 17.6	12.5
OH-coil stray vertical field (mT)[b]	1.92[c]	0.43[c]
OH-coil transparency (%)	67.2	63.

(a) Mean steady-state values.

(b) Back-bias values for a symmetric bipolar swing.

(c) Satisfies the stray-vertical-field constraint (< 2.45 mT, Section 6.2).

Table 4.5-VII.

PARAMETERS OF TITAN-II POLOIDAL-FIELD COILS

Coil	R (m)	$\pm z$ (m)	ΔR (m)	Δz (m)	$I^{(a)}$ (MA)	$j^{(a),(b)}$ (MA/m^2)	Mass$^{(c)}$ (tonne)	Turns
Trim	5.6600	0.8500	0.2500	0.2000	0.	0.	12.98	10
EF	5.9356	2.3608	0.6000	0.8000	− 9.3021	19.38	130.68	22
OH-1	5.6598	1.3134	0.2500	0.6000	1.1730	7.82	38.94	20
OH-2	3.9978	1.6684	0.6000	0.3000	1.4076	7.82	33.01	24
OH-3	2.9896	1.4600	0.6500	0.3000	1.5249	7.82	26.74	26
OH-4	2.6200	1.1300	0.9500	0.3000	2.2287	7.82	34.25	38
OH-5	2.4200	0.6320	0.5500	0.6000	2.5806	7.82	36.63	44
OH-6	2.4200	0.1500	0.5500	0.3000	1.2903	7.82	18.31	22

(a) Mean steady-state values for the EF coils and back-bias values for the OH coils for a symmetric bipolar swing.

(b) Averaged over the entire coil cross section.

(c) A density of 7.3 tonne/m^3 is assumed.

Table 4.5-VIII.

CIRCUIT PARAMETERS FOR TITAN-II PF-COIL DESIGNS[a]

Self inductances (μH)	
· L_p	13.29
· L_{OH}	3.68
· L_{EF}	13.35
· L_{trim}	19.35
Mutual inductances (μH)	
· $M_{OH,p}$	3.92
· $M_{OH,EF}$	3.04
· $M_{OH,Trim}$	4.03
· $M_{EF,p}$	4.12
· $M_{EF,Trim}$	8.22
· $M_{Trim,p}$	6.15
Current levels (MA-turn)	
· I_ϕ	17.82
· I_{EF}	18.60
· ΔI_{OH}	40.82
Magnetic fluxes (Wb)	
· Plasma	236.9
· EF coil	77.1
· OH coil	159.8

(a) Equivalent single-turn inductance values are given.

Table 4.5-IX.

PARAMETERS OF TITAN-II PF-COIL DESIGNS

EF-coil current (MA-turn)[a]	18.6
EF-coil volume (m^3)	35.8
EF-coil mass (tonne)	261.4
EF-coil peak field (T)[a]	7.2
EF-coil current density (MA/m^2)[a]	19.4
Vertical field index, n	0.40
OH-coil current (MA-turn)[b]	20.4
OH-coil volume	51.5
OH-coil mass (tonne)	375.8
OH-coil joule losses (MW)[b]	52.5
OH-coil von Mises stress (MPa)[b]	33.4
OH-coil peak field (T)[b]	4.7
OH-coil current density (MA/m^2)[b]	7.8
OH-coil stray vertical field (mT)[b]	2.30[c]

(a) Mean steady-state values.

(b) Back-bias values for a symmetric bipolar swing.

(c) Satisfies the stray-vertical-field constraint (< 2.45 mT, Section 6.2).

4.6. EQUILIBRIUM-FIELD (EF) COILS

4.6.1. Models and Constraints

Since the EF coils are continuously active, the recirculating power can be minimized by using superconducting EF coils. Superconducting EF coils, however, require $\sim 1.5\,\mathrm{m}$ of blanket and shielding between the coils and plasma compared to ≤ 0.4 to $0.8\,\mathrm{m}$ for normal-conducting EF coils; hence, more current is needed to produce the same field resulting in an increase in the stored energy and a more massive and expensive coil set. The trade-off between normal-conducting and superconducting EF coils was examined and found to weigh slightly in favor of superconducting EF coils (Section 3.4). Consequently, the use of superconducting EF coils is adopted for the TITAN reactor study. An additional constraint is imposed of using only a single pair of EF coils positioned not to interfere with vertical or horizontal movement of the first wall, blanket, shield, and TF-coil assembly during maintenance procedures. This EF-coil set would be a life-of-plant item.

The steady-state EF-coil currents are determined by equating the on-axis vacuum field produced by the EF coil to the vertical field required for toroidal equilibrium. The required vertical field, B_V, is given by [3,4]

$$B_V = \frac{\mu_o I_\phi}{4\pi R_T}\left[\ln\left(\frac{8R_T}{r_p}\right) + \frac{l_i}{2} + \beta_\theta - 1.5\right], \tag{4.6-1}$$

where R_T and r_p are the plasma major and minor radii, respectively, I_ϕ is the steady-state plasma current, β_θ is the poloidal beta, and l_i is the internal inductance per unit length of plasma. Typically, $l_i \simeq 1$ for RFP field and current profiles. The position of the EF coils is determined such that the value of the decay index,

$$n \equiv \frac{\partial(\ln B_V)}{\partial(\ln R)} \simeq \frac{R_T}{r_p}\,\frac{B_V\,(R_T - r_p) \;-\; B_V\,(R_T + r_p)}{B_V\,(R_T - r_p) \;+\; B_V\,(R_T + r_p)}, \tag{4.6-2}$$

remains in the range $0 \leq n \leq 1.5$ [5]. Having a circular plasma cross section further constrains the index [4] to $0 < n \leq 0.65$, which is the criterion used herein.

During the plasma start-up, an additional EF-trim coil is required to ensure the plasma remains in equilibrium, as is discussed in Section 6.3. Furthermore, the reactive power associated with maintaining the plasma in equilibrium during oscillating-field current-drive (OFCD) is substantially reduced if the applied voltage is held fixed on the superconducting EF coil and the OFCD transient is followed with the EF-trim coil, as is

described in Section 7.4. The current requirements of the trim coil are small (~ 1 MA), permitting a normal-conducting Cu-alloy trim coil. Furthermore, the equilibrium field and the decay index are relatively insensitive to the position of the trim coils. Consequently, the trim-coil positions are determined primarily by the requirements for vertical access.

4.6.2. EF-Coil Design

The TITAN-I EF- and trim-coil design is shown in Figure 4.5-7 and described in Tables 4.5-IV through 4.5-VI. The steady-state flux contours shown in Figure 4.6-1 indicate that the liquid-Li flow paths in the TITAN-I blanket and shield flow parallel to the dominant poloidal field. An inverse minor-radius dependency of the poloidal-field magnitude was assumed to determine the MHD pressure drops associated with the liquid-Li flow paths described in Section 10; this dependency is consistent with the steady-state magnetic-field-strength plot in Figure 4.6-1.

The TITAN-II EF- and trim-coil design is shown in Figure 4.5-9 and described in Tables 4.5-VII through 4.5-IX. The TITAN-II design is similar to the TITAN-I but the coils are closer to the plasma. Consequently, the EF-coil current for TITAN-II is smaller than for TITAN-I (18.6 compared with 19.2 MA for TITAN-I) and the inductive coupling of the TITAN-II EF coils to the plasma is better (77.1 Wb compared with 74.5 Wb for TITAN-I).

4.7. SUMMARY AND CONCLUSIONS

Two distinct coil designs were developed for the TITAN reactor to demonstrate that a range of designs are capable of efficient, high-mass-power-density operation. A comparison between the TITAN-I and TITAN-II coil designs made solely on the basis of magnetics performance is not appropriate, because other subsystems play an equally important role in determining the overall reactor performance as measured by the COE or the plant capital cost (Section 3.4). Both TITAN-I and TITAN-II coil designs are characterized by operation at low fields (≤ 6 T for copper-alloy OH coils and < 8 T for superconducting EF coils) and stresses (≤ 100 MPa). The only major development area envisioned is the demonstration of divertors in RFPs, which should begin with the next generation of RFP experiments [10]. The design constraints imposed generally were met by a wide margin in a range of design options, with the exception of the vertical-stack OH-coil configuration. This design margin facilitates the integration of the coil sets into the

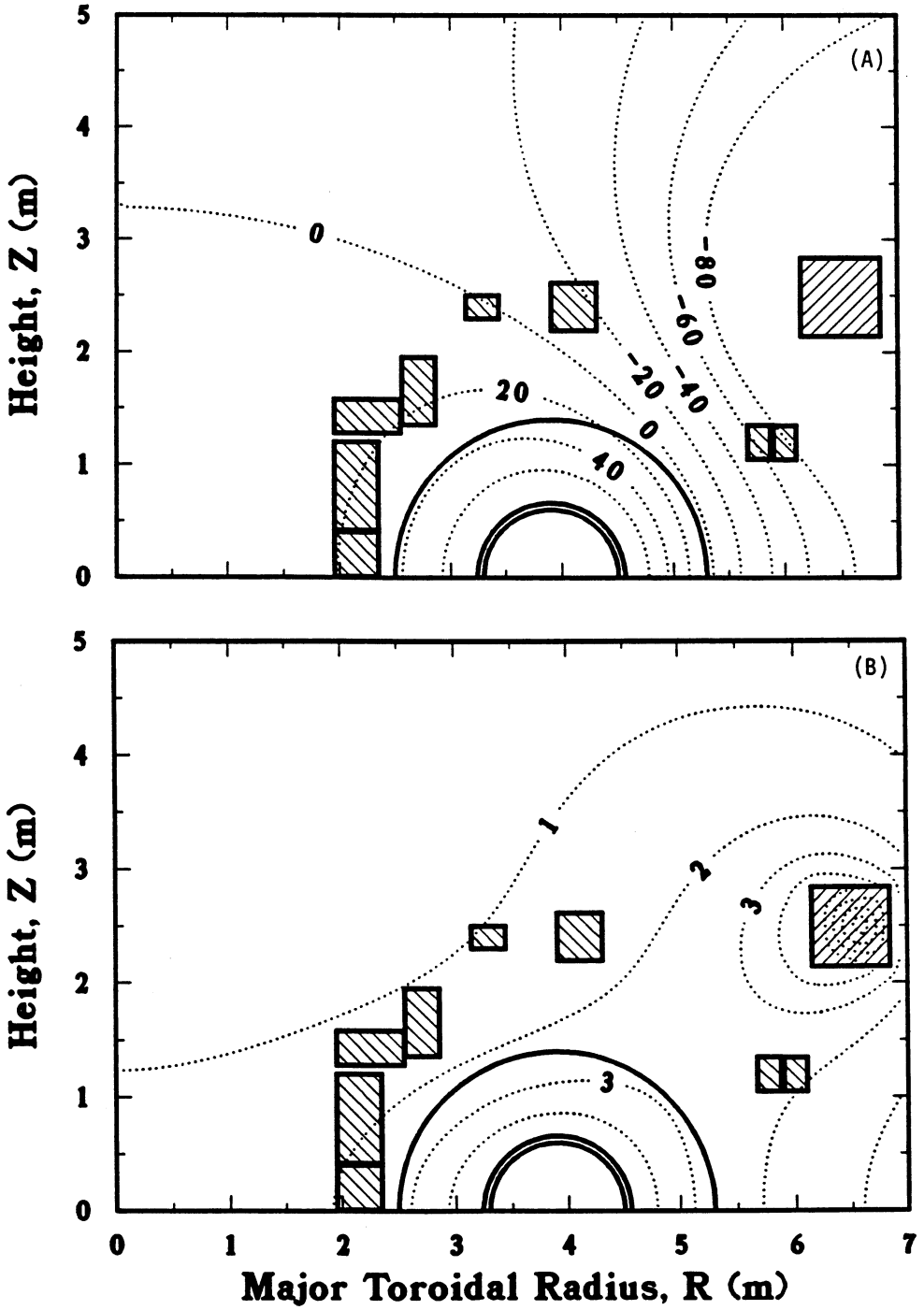

Figure 4.6-1. Contour plots of flux (A) and magnetic-field strength (B) for the EF coils and plasma at steady-state current for TITAN-I. The flux contours are labeled in weber and the magnetic-field contours are labeled in tesla.

overall reactor torus design. Additionally, non-magnetic considerations such as safety (*e.g.*, He-cooled OH coils), economics (*e.g.*, TF IBCs that recover ohmic losses), and maintenance (*e.g.*, non-interfering EF-coil locations) were included as major constraints of the overall design.

REFERENCES

[1] D. Steiner, R. C. Block, and B. K. Malaviya, "The Integrated- Blanket- Coil Concept Applied to the Poloidal Field and Blanket Systems of a Tokamak Reactor," *Fusion Technol.* **7** (1985) 66.

[2] R. L. Hagenson, R. A. Krakowski, C. G. Bathke, R. L. Miller, M. J. Embrechts, *et al.*, "Compact Reversed-Field Pinch Reactors (CRFPR): Preliminary Engineering Considerations," Los Alamos National Laboratory report LA-10200-MS (August 1984).

[3] V. D. Shafranov, "Plasma Equilibrium in a Magnetic Field," *Reviews of Plasma Physics,* Vol. 2, Consultant Bureau, New York (1966) p. 103.

[4] J. M. Greene, J. L. Johnson, and K. E. Weimer, "Tokamak Equilibrium," *Phys. Fluids* **14** (1971) 671.

[5] V. S. Mukhovatov and V. D. Shafranov, "Plasma Equilibrium in a Tokamak," *Nucl. Fusion* **11** (1971) 605.

[6] D. Steiner, M. J. Embrechts, R. Mohanti, and W. Kelleher, "The Integrated-Blanket-Coil Concept Applied to the Spherical Torus," *Proc. 11th Symp. on Fusion Eng.*, Austin, TX (November 1985) 530.

[7] H. A. Bodin, R. A. Krakowski, and O. Ortolani, "The Reversed-Field Pinch: from Experiment to Reactor," *Fusion Technol.* **10** (1986) 307.

[8] R. L. Spencer, "Magnetic Islands and Stochastic Field Lines in the RFP," *Proc. RFP Theory Workshop,* Los Alamos, NM (April 29 - May 2, 1980), Los Alamos National Laboratory report LA-8944-C (January 1982) 129.

[9] J. B. Taylor, "Relaxation of Toroidal Plasma and Generation of Reversed Magnetic Field," *Phys. Lett.* **33** (1974) 1139.

[10] P. Thullen and K. Schoenberg (Eds.), "ZT-H Reversed-Field Pinch Experiment Technical Proposal," Los Alamos National Laboratory report LA-UR-84-2602 (1984) 26.

[11] R. L. Miller, C. G. Bathke, R. A. Krakowski, F. M. Heck, L. Green, J. S. Karbowski, *et al.*, "The Modular Stellarator Reactor: A Fusion Power Plant," Los Alamos National Laboratory report LA-9737-MS (July 1983).

[12] S. J. Sackett, "EFFI - A Code for Calculating the Electromagnetic Field, Force, and Inductance in Coil Systems of Arbitrary Geometry - User's Manual," Lawrence Livermore National Laboratory report UCID-17621 (1977).

[13] C. G. Bathke and R. A. Krakowski, "A Comparison Study of Toroidal-Field and Bundle Divertors for a Compact Reversed-Field Pinch Reactor," *Fusion Technol.* **8** (1985) 1616.

[14] C. G. Bathke, R. L. Miller, and R. A. Krakowski, "Magnetic Divertor Design for the Compact Reversed Field Pinch Reactor," *Proc. 13th Symp. on Fusion Tech.*, Varese, Italy (September 1984) 1259.

[15] C. Copenhaver, R. A. Krakowski, N. M. Schnurr, R. L. Miller, C. G. Bathke, R. L. Hagenson, *et al.*, "Compact Reversed-Field Pinch Reactors (CRFPR): Fusion-Power-Core Integration Study," Los Alamos National Laboratory report LA-10500-MS (August 1985).

[16] K. A. Werley, C. G. Bathke, and R. A. Krakowski, "Edge Plasmas and Plasma/Wall Interactions in an Ignition-Class Reversed Field Pinch," in *Proc. 12th IEEE Symp on Fusion Eng.*, Monterey, CA (October 1987).

[17] R. W. Moses, Jr. and J. K. Ballou, "Inductive Shielding for Pulsed Energy Storage Magnets," *IEEE Trans. on Magnetics* **MAG-11** (1975) 493.

[18] W. R. Smyth, *Static and Dynamic Electricity,* McGraw-Hill Book Company, NY (1939).

[19] F. Najmabadi, "Computing Magnetic Field, Vector Potential, and Inductance of Circular Coils with Rectangular Cross Section," University of California Los Angeles report UCLA-PPG-1255 (1989).